CCIT Report #490 June 2004

A Maximum Likelihood Approach to Spatial Compounding of Ultrasound Images

Yair Kerner and Moshe Porat

Department of Electrical Engineering
Technion – Israel Institute of Technology
Haifa 32000, Israel

Abstract

We develop a new method to exploit pairs of ultrasound scans of the same image plane with the aim of enhancing the quality of ultrasound imaging. Each image pair is assumed to be co-registered with 90° separation between the two insonification directions. The motivation for such spatial compounding is the resolution in medical ultrasound imaging, which is significantly worse in the lateral (transverse) direction compared to the axial (longitudinal) direction. The proposed method seeks a Maximum-Likelihood solution for the identification of the system response and the noise variance through the Expectation-Maximization technique, similar to the approach of multi-channel image restoration (MCIR). For the following step of image reconstruction and compounding we take into account the non-linear operations of envelope detection and log-compression that are required for the display of ultrasound images. We show that the best ability to separate close small objects is achieved when the compound image is produced through first using separate Wiener filtering for each RF image, afterwards performing envelope-detection and finally averaging the two envelope-detected images.

Corresponding author:
Moshe Porat,
Dept. of Electrical Engineering,
Technion, Haifa 32000, Israel.
Email: mp@ee.technion.ac.il
Fax: +972-4-832-3041
Tel.: +972-4-829-4684

1 Introduction

Medical ultrasound images are produced from echoes reflected from biological tissue, and are considered as a blurred version of the tissue reflectivity with significantly worse resolution in one direction compared to the perpendicular direction. The model that is commonly used in ultrasound imaging research for the relation between the received signal and the tissue reflectivity is of a linear space-invariant system (LSI). Handling space variations of the Point Spread Function (PSF) is usually through partitioning the imaged plane to smaller regions with approximately invariant PSF.

For more than two decades various algorithms have been suggested to sharpen the images, either by deconvolution assuming the PSF is known [1], [2] or using blind deconvolution [3], [4], [5], [6], [7], [8], [9], [10]. The prevalent approach in researches of blind deconvolution for ultrasound images is to use the LSI method of Wiener filter to recover the reflectivity image, and therefore most of the effort is concentrated in estimating the PSF. It is worth noting that while a few algorithms used the envelope-detected and log-compressed image as their input [1], [2], in most of the published work deconvolution is applied to the RF image [3]-[10].

In the recent decade several authors [11], [12], [13], [14], [15], [16], [17] developed algorithms for compounding of ultrasound images of the same region from different angles. These algorithms have a similar structure: First, envelope detection is performed for each scan; then, each scan is rotated to align with a reference coordinate system and the original image values are interpolated to determine the values on the joint sampling grid; finally the compound image is created through combination of the values at each pixel of the joint sampling grid from all the separate images.

In parallel, researchers who sought ways to overcome blur phenomena of photographic images developed algorithms for multi-channel image restoration. Ghiglia [18] presented a constrained least-squares algorithm for image restoration given several blurred images of the same object, each corresponding with a different PSF. Later, Katsaggelos et al. [19] presented a systematic framework for performing multi-channel image restoration in the frequency domain. In the field of medical imaging this method was applied to dual-radionuclide imaging [20]. Tom et al. [21] established a maximum-likelihood formulation for the general problem of multi-channel image restoration, and utilized the expectation-maximization algorithm to solve it.

To the best of our knowledge no algorithm was developed to exploit both deconvolution and compounding for ultrasound image applications. When considering multi-channel image restoration algorithms for the field of ultrasound images, one must note fundamental differences from the field of photographic images in several characteristics of the problem: the system response has band-pass behavior in one dimension rather than low-pass in both dimensions, the sampling intervals are different in each direction, and non-linear operations are involved in the display procedure.

The research that is presented in this paper is a milestone in a long-term research for improvement in the quality of ultrasound images by combining the information from imaging of the same plane from different view directions. This paper aims at achieving an enhanced ultrasound image compared to images from single scans through exploiting pairs of ultrasound scans of the same plane. Each pair is assumed to consist of two co-registered images with 90° separation between their insonification directions and without deformations due to variations in the speed of sound. In order to allow usage of different view directions of a plane within a 3 dimensional space careful calibration of the transducer's location is needed, and in addition pre-processing might be required to accomplish co-registration.

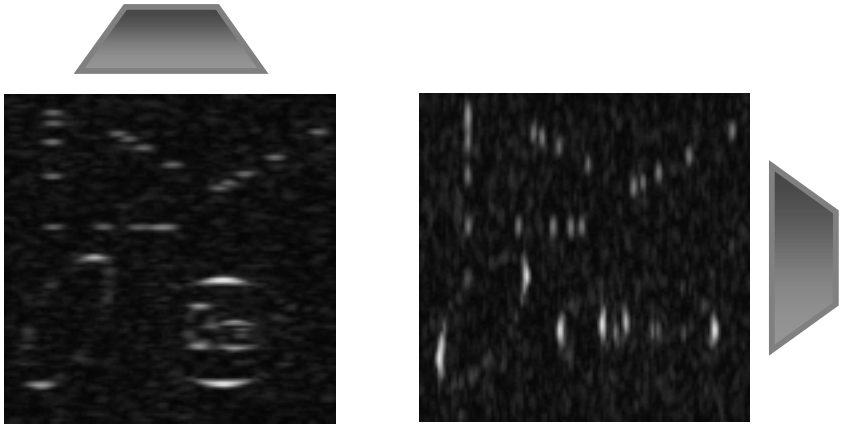

Figure 1.1: A simulated pair of ultrasound images of the same plane at 90° separated views.

This paper is organized as follows. Section 2 is an overview of ultrasound imaging and the basic terms in this field. Section 3 describes the mathematical model for image formation that is the basis for the development of the main algorithm. The model covers the tissue reflectivity, the degradation process, 90° rotation and transformation to the frequency domain. Section 4 details the algorithm for identification of the system parameters. Section 5 describes methods for image restoration and compounding for a given estimation of the system parameters. Section 6 summarizes the paper and depicts directions for future research that can be based on this paper.

2 Ultrasound Imaging

In medical ultrasound imaging short pulses of compressional waves are emitted from a *transducer* that is made of an array of resonant elements [22]. Each element is made of a piezoelectric material that vibrates at its resonance frequency, normally in the range of 2-10 MHz, when a voltage is applied to it. The emitted pulses pass through a coupling gel and travel through a biological tissue. The propagation velocity of the ultrasound pulses depends on the biological contents such as blood, fat or muscle, and it is usually in the range of 1400-1600 m/sec. The mean sound velocity in human tissue is usually taken to be 1540 m/sec.

Acoustic energy returns to the transducer through two main mechanisms related to changes in the tissue density or compressibility. *Specular reflection* takes place if such change is across a boundary significantly large in extent with respect to the wavelength of the pulse. If the incident wave is not normal to the interface between the two media, the transmitted wave will be refracted according to Snell's law. *Scattering* occurs when acoustic waves interact with objects of size comparable to or less than the wavelength, as they tend to reflect weak waves in all directions. A volume of scatterers, like blood cells or organ tissue, will act as a diffuse reflector. Since array imaging relies on coherent illumination and detection, the result of such diffuse reflections is appearance of random-like bright and dark spots in the image known as *speckle*.

There are several types of transducer arrays, and each is suitable for imaging of different organs in the body. An *annular array* consists of concentric piezoelectric rings and requires mechanical scanning in order to form an image. A *linear array* is constructed of a row of elements, usually between 48-200, along a straight line. A *curved linear array* is composed of a similar row of elements but along an arc forming a convex probe, giving a wider field of view.

If all the elements in an array are excited simultaneously, the resulting wave will travel perpendicular to the surface of the array. However, if the excitation occurs with certain delays

among the elements, the effects of *beam steering* and *transmit focusing* can be achieved. In addition, the transmission can include *apodization*, which is a weighting of the contribution of the different elements such that the central elements has a higher gain and it is gradually attenuated when approaching the outer elements. This allows control of the level of the side lobes of the beam. The wave that arrives back at the transducer is converted to electronic signals by the piezoelectric elements. Beam steering, receive focusing and apodization can be introduced as part of the signal reception in a similar manner as is done for transmission. The resulting signal, which is digital at sample rate of about 20 MHz, is called the *RF signal*.

The key signal-processing operations that are applied to the received RF signal for each beam separately are envelope detection and compression. *Envelope detection* can be done either through Hilbert filtering followed by absolute value calculation or through demodulation followed by low-pass filtering and absolute value calculation. *Compression* is a mapping of the signal levels, such as a logarithmic function, which reduces the dynamic range, so that the weak echoes can be visualized together with strong ones. A side effect is that fewer bits, usually 8, are required for pixel representation.

Two-dimensional ultrasound images, known as brightness mode or *B-mode scans*, can be achieved in a number of ways. A *phased array scan* is generated by a linear array with a relatively small aperture, e.g. 15 mm, of which all the elements are used such that the ultrasound beams are emanating from one point and steered in a sector. Such scans are normally used in cardiology applications, where small aperture is needed to access between the ribs, and in deep abdominal exams. A *linear array scan* is generated by a linear array with a larger aperture, around 40 mm, of which only a subset of the elements is used to generate a beam, such that the subsets are gradually switched and the beam is swept from one side of the array to the other. The resulting image has the shape of a rectangle or parallelogram. These scans are used in a variety of abdominal, peripheral and small-parts exams. Curved linear array probes can be operated with the sweeping technique of linear array scans, but due to the probe curvature the resulting image has the shape of a sector resembling that of a phased array scan.

Except for the case of linear array scan, data is collected in a polar coordinate system. In order to prepare the image for display, this requires *scan conversion*, which is a transform from r-θ coordinates to Cartesian followed by interpolation to generate samples on a rectangular grid.

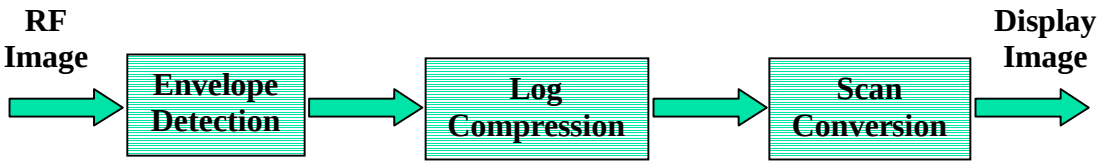

Figure 2.1: Elementary signal processing modules of a B-mode scan system.

3 Mathematical Model of the Problem

3.1 Notation

A 2-D spatial location in the imaging plane is denoted as (x, z), where x is the coordinate in the lateral direction and z is the coordinate in the axial direction. In the frequency domain (ω_x, ω_z) represents the spatial frequency in radians. Whenever matrix representation is used the

axial direction is column-wise unless stated otherwise. When matrix coordinates appear in parentheses the first parameter specifies the horizontal coordinate $\mathbf{A}(m, n) = \mathbf{A}_{nm}$ in order to keep consistency between matrix and 2-D signal or image formulations.

Here, *image* and *2-D signal* are used as synonyms. The matrix **R** indicates the unknown tissue reflectivity in the imaging plane. The matrix **S** denotes the observed RF image, which is the collection of sampled signals from all the transducer elements during a single scan.

3.2 Tissue Reflectivity Model

The tissue reflectivity can be considered as resulting from an assembly of reflectors and scatterers [7], [10]. As is mentioned in Section 2, a reflector is an interface, large compared with the wavelength of the ultrasonic pulse, typically attributable to boundaries between regions of different tissue types. The resulting specular reflections depend on the region boundary orientation and the acoustic impedance of each region. On the other hand, scatterers are objects, small compared with the wavelength, characteristically diffused within the tissue and induce a speckle pattern in B-mode images.

For that reason, and following [7], the tissue reflectivity is modeled in this work as the sum of a deterministic function **D** representing the specular reflections and a zero-mean Gaussian stochastic process **U** corresponding with the speckle component:

$$\mathbf{R}(x, z) = \mathbf{D}(x, z) + \mathbf{U}(x, z) \tag{3.1}$$

3.3 Degradation Model

The interaction of the ultrasonic pressure field with the tissue is 3-dimensional, but its observation in B-mode imaging is a 2-D space. Subject to customary assumptions, the formation process of the RF image can generally be modeled as a 2-D spatial linear filtering operation with a spatially variant point-spread function [5], [6], [7], [23], [24]. It is possible to segment the image into regions for which the PSF remains constant and simple convolution describes with good accuracy the image formation:

$$\mathbf{S}(x, z) = \mathbf{P}(x, z) * \mathbf{R}(x, z) + \mathbf{N}(x, z) \tag{3.2}$$

where $*$ denotes 2-D convolution, **P** represents the PSF and **N** represents additive noise. The noise term is modeled as a white zero-mean Gaussian random process that is independent of the tissue reflectivity and the PSF [5]-[7].

(a) (b)

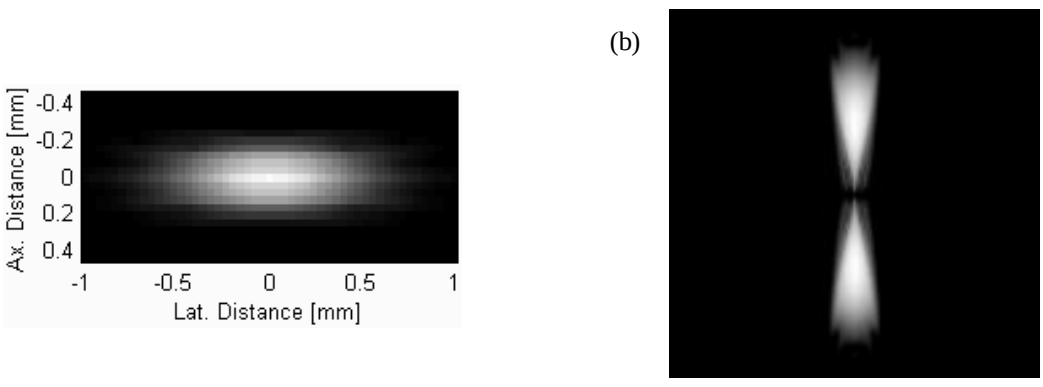

Figure 3.1: Simulated system response using the model in [24] with the axial direction along the vertical axis: (a) PSF envelope. (b) Frequency response. In both frequency axes the range is $[-\pi, \pi]$ rad.

The system response in the frequency domain $\mathbf{P}(\omega_x, \omega_z)$ is related to the PSF through 2-D Fourier transform. In the axial dimension the system response behaves as a band-pass filter, while in the lateral dimension it can be considered as a low-pass filter [24], as illustrated in Figure 3.1. The resolution in the lateral direction is significantly worse than the axial resolution as the PSF has wide extent laterally and narrow support axially. Equivalently, the system response has much smaller bandwidth in the lateral dimension than in the axial dimension.

3.4 90° Rotation in Space and Frequency Domains

In this paper rotation is treated as positive when its direction is from the positive ray of the *x*-axis toward the positive ray of the *z*-axis, and as negative when it is in the opposite direction. This implies that if conventional matrix coordinates are employed then positive rotation is clockwise.

Let $\mathbf{A}_1$ and $\mathbf{A}_2$ denote two RF images that were recorded with $\mathbf{A}_2$ taken after the transducer was turned by –90° relative to its direction during the recording of $\mathbf{A}_1$. The superscript $^{\text{rot}}$ is used to indicate 90° rotation, while $^{\text{inv-rot}}$ indicates –90° rotation. Assuming that the tissue reflectivity $\mathbf{R}$ is the same for both recordings, then:

$$\begin{aligned} \mathbf{A}_1 &= \mathbf{P}_1 * \mathbf{R} + \mathbf{N}_a \\ \mathbf{A}_2 &= \mathbf{P}_2 * \mathbf{R}^{\text{inv-rot}} + \mathbf{N}_b \end{aligned} \tag{3.3}$$

where $\mathbf{P}_1$, $\mathbf{P}_2$ denote the system's PSF in each case and $\mathbf{N}_a$, $\mathbf{N}_b$ denote the additive noise. Rotating $\mathbf{A}_2$ in equation (3.3) by 90° to get: $\mathbf{A}_2^{\text{rot}} = \mathbf{P}_2^{\text{rot}} * \mathbf{R} + \mathbf{N}_b^{\text{rot}}$, and substituting: $\mathbf{S}_V \equiv \mathbf{A}_1$, $\mathbf{S}_H \equiv \mathbf{A}_2^{\text{rot}}$, $\mathbf{N}_1 \equiv \mathbf{N}_a$ and $\mathbf{N}_2 \equiv \mathbf{N}_b^{\text{rot}}$, yields:

$$\begin{aligned} \mathbf{S}_V &= \mathbf{P}_1 * \mathbf{R} + \mathbf{N}_1 \\ \mathbf{S}_H &= \mathbf{P}_2^{\text{rot}} * \mathbf{R} + \mathbf{N}_2 \end{aligned} \tag{3.4}$$

In other words, due to the rotation to a joint coordinate system the blur is treated as rotated by 90° instead of regarding the image as rotated by –90°. Note that for $\mathbf{S}_V$ the axial direction coalesces with the vertical direction, while for $\mathbf{S}_H$ it is horizontal. Therefore, according to the degradation model, $\mathbf{R}$ is more blurred horizontally to generate $\mathbf{S}_V$ and more blurred vertically to generate $\mathbf{S}_H$.

The 90° rotation operator in infinite 2-D space $^{\text{rot}}: \mathbb{S}^2 \rightarrow \mathbb{S}^2$ is equivalent to inversion of the *z*-axis followed by axes interchange, specifically given any function $f(x, z)$:

$$g(x', z') = f^{\text{rot}} = f(z', -x') \tag{3.5}$$

Applying Fourier transform, the same relation holds in the frequency domain as well [24]:

$$G(\omega_x', \omega_z') = \text{FT}\{ f^{\text{rot}} \} = \text{FT}\{ f \}^{\text{rot}} = F(\omega_z', -\omega_x') \tag{3.6}$$

where F and G are the Fourier transform (FT) of f and g respectively.

When dealing with matrices and DFT, rotation should be given special attention as straightforward 90° rotation results in a phase shift in the frequency domain.The property in equation (3.6) is maintained if the definition of 90° rotation utilizes the periodicity of the DFT:

$$\mathbf{B}(m', n') = \mathbf{A}^{\text{rot}} \equiv \mathbf{A}(n', [N-m']_{\text{mod } N}) \qquad , \qquad m' = 0, 1 \ldots N-1 \tag{3.7}$$

where $\mathbf{A}$ is a matrix with N rows. This is equivalent to column-wise inversion excluding the first row followed by transposition or alternatively transposition followed by row-wise inversion. Naturally, rotation by –90° is defined as the same set of operations carried out in inverse order.

3.5 Sampling Grid

We assume that the ultrasonic B-mode scan is performed as a linear-array scan. Hence, the sampling grid is rectangular, but the sampling intervals are different in each direction. The lateral sampling interval d_L is a consequent of the spacing between the piezoelectric crystals, which is in the region of few hundreds of μm. The axial sampling interval d_A is related to the sampling frequency f_S at the receiver and the speed of sound v within the tissue through:

$$d_A = \tfrac{1}{2}\, v / f_S \tag{3.8}$$

since the ultrasonic wave travels the distance between the crystal and the imaged object twice. For example, if $v \cong 1{,}540$ m/sec and $f_S = 20$ MHz [2]-[4], then $d_A \cong 38.5$ μm, and assuming $d_L = 500$ μm [1], the ratio between the lateral and axial sampling intervals is about 13:1. If $f_S = 10.5$ MHz [8] and the crystal spacing is approximately 200 μm [13], this ratio drops off to around 3:1.

Taking into account the different sampling intervals and treating the matrices of the reflectivity **R** and the PSF **P** as samples on a square grid with intervals d_A in both directions, the discrete-space LSI model for the generation of the 2 source images $\mathbf{S}_V$ and $\mathbf{S}_H$ from the tissue reflectivity **R** is:

$$\begin{aligned} \mathbf{S}_V &= (\mathbf{P}_1 * \mathbf{R}) \downarrow_H K + \mathbf{N}_1 \\ \mathbf{S}_H &= (\mathbf{P}_2^{\,rot} * \mathbf{R}) \downarrow_V K + \mathbf{N}_2 \end{aligned} \tag{3.9}$$

where $\downarrow_H K$ denotes horizontal decimation by factor K and $\downarrow_V K$ stands for vertical decimation.

3.6 Frequency Domain

Since multiplication in the discrete frequency domain is related to cyclic convolution in the discrete space domain, there is a need for zero padding before performing DFT on an expression with linear convolution. For 2 elements of lengths l_a and l_b the length of zero padding should be at least l_b–1 and l_a–1 respectively, such that the resulting total lengths are equal and at least l_a+l_b–1.

In order to avoid unnecessary complications to the mathematical expressions we utilized the following requirement: If **I** is the identity PSF, i.e. a Kronecker delta function at the origin, and $\mathbf{S} = \mathbf{R} * \mathbf{I}$, then in the frequency domain $\mathbf{S}(\omega_x, \omega_z) = \mathbf{R}(\omega_x, \omega_z)$ should hold for all ω_x and ω_z without phase shift. Consequently, the non-causal parts of any matrix that represents a PSF are folded to the end of that matrix due to the cyclic nature of the DFT.

For example, let $\mathbf{P}_1$ and $\mathbf{P}_2$ be rectangular matrices of size $l_z \times l_x$, let $\mathbf{S}_V$ and $\mathbf{S}_H$ be matrices of size $m_z \times m_x$, and let **R** be a square matrix of size $n \times n$. If the DFT of each of these matrices is a square matrix of size $N_{DFT} \times N_{DFT}$ ($N_{DFT} \geq \max(l_z+m_z-1,\ l_x+m_x-1)$), then the following relations hold:

$$\begin{aligned} \mathbf{S}_V &= \mathrm{DFT}\{\mathbf{S}_V \text{ zero-padded at its end with } (N_{DFT}-m_z) \text{ rows and } (N_{DFT}-m_x) \text{ columns}\} \\ \mathbf{S}_H &= \mathrm{DFT}\{\mathbf{S}_H \text{ zero-padded at its end with } (N_{DFT}-m_z) \text{ rows and } (N_{DFT}-m_x) \text{ columns}\} \end{aligned} \tag{3.10}$$

$$\mathbf{R} = \textit{Beginning}\ \{\ \mathrm{IDFT}\ \{\ \mathbf{R}\ \}\ \} \tag{3.11}$$

where $\mathbf{S}_V$, $\mathbf{S}_H$ and **R** are respectively the 2-D DFT's of $\mathbf{S}_V$, $\mathbf{S}_H$ and **R**, and *Beginning*{ **A** } means taking only the first n rows and first n columns of the matrix **A**. The unfolded PSF, namely with the origin at the center of the matrix, is retreived from the corresponding frequency response through:

$$\mathbf{P}_1 = \textit{Middle}\ \{\ \text{FFT-Shift}\ \{\ \text{IDFT}\ \{\ \mathbf{P}_1\ \}\ \}\ \} \tag{3.12}$$
$$\mathbf{P}_2 = \textit{Middle}\ \{\ \text{FFT-Shift}\ \{\ \text{IDFT}\ \{\ \mathbf{P}_2\ \}\ \}\ \}$$

where $\mathbf{P}_1$, $\mathbf{P}_2$ are the 2-D DFT's of $\mathbf{P}_1$, $\mathbf{P}_2$, FFT-Shift{ **A** } means swapping the first $\frac{1}{2}N_{DFT}$ rows/columns with the last $\frac{1}{2}N_{DFT}$ rows/columns of the matrix **A**, and *Middle*{ **A** } means taking only l_z rows and l_x columns from the matrix **A** where the resulting matrix is co-centric with **A**.

DFT of (3.12) with the above-mentioned zero-padding gives:

$$\mathbf{S}_V(\omega_x, \omega_z) = \mathbf{P}_1(\omega_x, \omega_z)\, \mathbf{R}(\omega_x, \omega_z) + \mathbf{N}_1(\omega_x, \omega_z) \tag{3.13}$$
$$\mathbf{S}_H(\omega_x, \omega_z) = \mathbf{P}_2(\omega_z, -\omega_x)\, \mathbf{R}(\omega_x, \omega_z) + \mathbf{N}_2(\omega_x, \omega_z)$$

where $\mathbf{N}_1$ and $\mathbf{N}_2$ are the 2-D DFT's of $\mathbf{N}_1$ and $\mathbf{N}_2$ correspondingly. Note, that all the elements in (3.13) are square matrices of size $N_{DFT} \times N_{DFT}$.

Using the vector notation $\mathbf{s}_{k,l} \equiv \begin{pmatrix} \mathbf{S}_V(\omega_x,\omega_z) \\ \mathbf{S}_H(\omega_x,\omega_z) \end{pmatrix}$, $\mathbf{h}_{k,l} \equiv \begin{pmatrix} \mathbf{P}_1(\omega_x,\omega_z) \\ \mathbf{P}_2(\omega_z,-\omega_x) \end{pmatrix}$, $r_{k,l} \equiv \mathbf{R}(\omega_x, \omega_z)$, and $\mathbf{n}_{k,l} \equiv \begin{pmatrix} \mathbf{N}_1(\omega_x,\omega_z) \\ \mathbf{N}_2(\omega_x,\omega_z) \end{pmatrix}$, with $\omega_x = \frac{2\pi k}{N_{DFT}}$ and $\omega_z = \frac{2\pi l}{N_{DFT}}$, (3.13) can be compactly written as:

$$\mathbf{s}_{k,l} = \mathbf{h}_{k,l}\, r_{k,l} + \mathbf{n}_{k,l} \tag{3.14}$$

Equation (3.14) is schematically described in Figure 3.2.

The variable $r_{k,l}$ is stochastic with mean $d_{k,l} \equiv \mathbf{D}(\omega_x, \omega_z)$ and variance λ_u, and is assumed to have Gaussian probability density function (PDF) [7]. The noise term $\mathbf{n}_{k,l}$ is a random vector with zero mean and a diagonal 2×2 covariance matrix $\mathbf{\Lambda}$, where the diagonal elements are the variances λ_1 and λ_2 of $\mathbf{N}_1(\omega_x, \omega_z)$ and $\mathbf{N}_2(\omega_x, \omega_z)$ respectively.

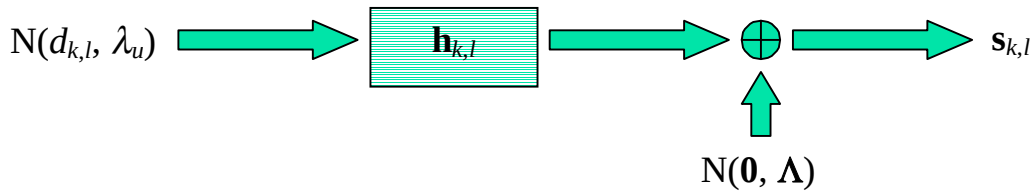

Figure 3.2: Schematic description of the model.

4 Maximum Likelihood Parameter Estimation

As explained in section 5, the band-pass nature of the ultrasonic system response and the subsequent envelope detection require separate treatment for the image reconstruction. Thus, the blind deconvolution problem is solved in two steps as illustrated in Figure 4.1:

1. Estimation of the parameters of the ultrasonic system: the system response, the noise variance and the speckle variance.
2. Image reconstruction with the estimated parameters and spatial compounding.

The estimation of the system response can be viewed as an optimization problem where we search for the unknown parameters of a PDF and for which the maximum-likelihood (ML) approach can be applied.

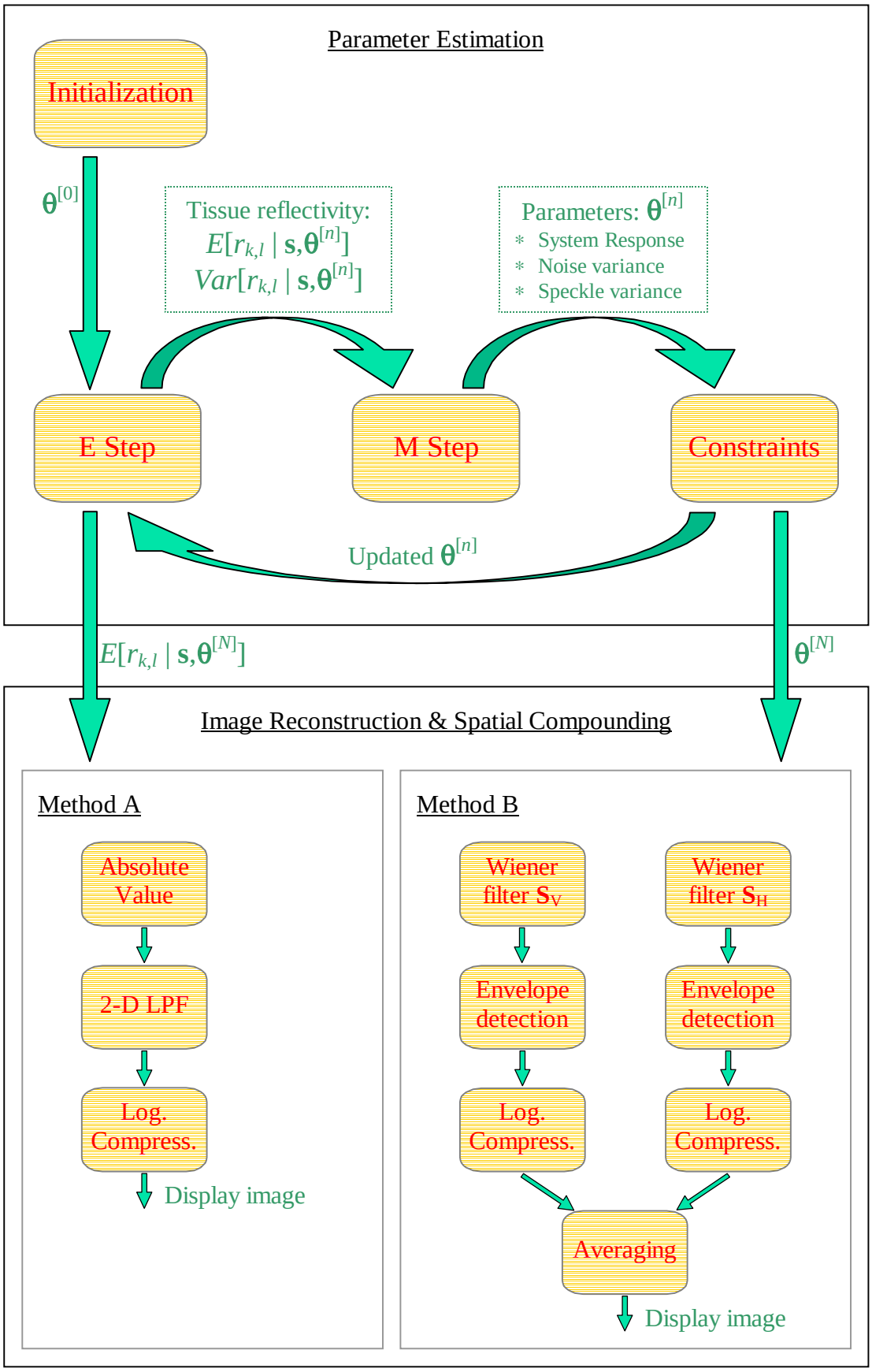

Figure 4.1: Flow diagram of the algorithm with the tissue reflectivity as the hidden data

If the speckle component in equation (3.1) and the noise terms in equation (3.13) are uncorrelated white Gaussian random processes, the observed RF image is also Gaussian with $\mathbf{s}_{k,l}$ having mean $\mathbf{h}_{k,l}\, d_{k,l}$ and covariance matrix $(\lambda_u\, \mathbf{h}_{k,l}\, \mathbf{h}_{k,l}^{\dagger} + \mathbf{\Lambda})$:

$$f(\mathbf{s}_{k,l} \mid \boldsymbol{\theta}_{k,l}) = |2\pi\, (\lambda_u\, \mathbf{h}_{k,l}\, \mathbf{h}_{k,l}^{\dagger} + \mathbf{\Lambda})|^{-½} \qquad (4.1)$$
$$\exp[-½\, (\mathbf{s}_{k,l} - \mathbf{h}_{k,l}\, d_{k,l})^{\dagger}\, (\lambda_u\, \mathbf{h}_{k,l}\, \mathbf{h}_{k,l}^{\dagger} + \mathbf{\Lambda})^{-1}\, (\mathbf{s}_{k,l} - \mathbf{h}_{k,l}\, d_{k,l})]$$

The parameter set of this PDF is: $\boldsymbol{\theta}_{k,l} \equiv [\mathbf{h}_{k,l}^{\mathrm{T}},\, d_{k,l},\, \lambda_u,\, \lambda_1,\, \lambda_2]^{\mathrm{T}}$.

The log-likelihood function is then:

$$L(\boldsymbol{\theta}) \equiv \ln \prod_k \prod_l f(\mathbf{s}_{k,l} \mid \boldsymbol{\theta}_{k,l}) = \sum_k \sum_l \ln f(\mathbf{s}_{k,l} \mid \boldsymbol{\theta}_{k,l}) = \qquad (4.2)$$
$$= -½ \sum_k \sum_l \ln |2\pi\, (\lambda_u\, \mathbf{h}_{k,l}\, \mathbf{h}_{k,l}^{\dagger} + \mathbf{\Lambda})|$$
$$-½ \sum_k \sum_l [\, (\mathbf{s}_{k,l} - \mathbf{h}_{k,l}\, d_{k,l})^{\dagger}\, (\lambda_u\, \mathbf{h}_{k,l}\, \mathbf{h}_{k,l}^{\dagger} + \mathbf{\Lambda})^{-1}\, (\mathbf{s}_{k,l} - \mathbf{h}_{k,l}\, d_{k,l})\,]$$

The ML estimate of the parameter set is the set that maximizes $L(\boldsymbol{\theta})$ in equation (4.2). Employing optimization of this direct likelihood function yields a difficult minimization problem, especially since the unknown quantities of reflectivity and blur are coupled through multiplication. The expectation-maximization (EM) algorithm [25] is an iterative technique that greatly simplifies the ML problem.

4.1 Maximum Likelihood with Expectation Maximization

According to the EM method, a set $\mathbf{y}$ called the *complete data* is defined such that it is not observed directly, but only by means of the *observed data* $\mathbf{s}$, which is related to $\mathbf{y}$ through a non-invertible linear mapping. Each iteration of the algorithm is composed of two steps: expectation (E step) and maximization (M step), as illustrated in Figure 4.1. In the E step the conditional expectation of $\ln\{f_{\mathbf{y}}(\mathbf{y}|\boldsymbol{\theta})\}$ is calculated, using the current estimates of the parameters $\boldsymbol{\theta}^{[n]}$ and conditioned upon the observed data:

$$Q(\boldsymbol{\theta}|\boldsymbol{\theta}^{[n]}) = E[\ln\{\, f_{\mathbf{y}}(\mathbf{y}|\boldsymbol{\theta})\, \} \mid \mathbf{s}, \boldsymbol{\theta}^{[n]}] \qquad (4.3)$$

In the M step the expectation $Q(\boldsymbol{\theta}|\boldsymbol{\theta}^{[n]})$ is maximized with respect to $\boldsymbol{\theta}$ to provide a new estimation of the parameters:

$$\boldsymbol{\theta}^{[n+1]} = \arg\max_{\boldsymbol{\theta}}\, Q(\boldsymbol{\theta}|\boldsymbol{\theta}^{[n]}) \qquad (4.4)$$

4.2 EM with the Reflectivity Image as the Hidden Data

4.2.1 The Complete Data

Let us define the complete data for the problem at hand as $\mathbf{y}_{k,l} = \begin{pmatrix} \mathbf{s}_{k,l} \\ r_{k,l} \end{pmatrix} = \begin{pmatrix} \mathbf{S}_{\mathrm{V}}(\omega_x, \omega_z) \\ \mathbf{S}_{\mathrm{H}}(\omega_x, \omega_z) \\ \mathbf{R}(\omega_x, \omega_z) \end{pmatrix}$,

so the non-invertible mapping is $\mathbf{s}_{k,l} = (\, \mathbf{I} \quad \mathbf{0}\,)\, \mathbf{y}_{k,l} = \begin{pmatrix} 1 & 0 & 0 \\ 0 & 1 & 0 \end{pmatrix} \begin{pmatrix} \mathbf{S}_{\mathrm{V}}(\omega_x, \omega_z) \\ \mathbf{S}_{\mathrm{H}}(\omega_x, \omega_z) \\ \mathbf{R}(\omega_x, \omega_z) \end{pmatrix}$. The unknown

quantity $r_{k,l}$ within the complete data is referred to as the *hidden data*. The system response, as part of the parameter set $\boldsymbol{\theta}_{k,l} \equiv [\mathbf{h}_{k,l}^{\mathrm{T}}, d_{k,l}, \lambda_u, \lambda_1, \lambda_2]^{\mathrm{T}}$, is the estimation target.

According to the conditional-probability formula $f_{\mathbf{a},\mathbf{b}}(\mathbf{a},\mathbf{b}) = f_{\mathbf{a}}(\mathbf{a})\, f_{\mathbf{b}|\mathbf{a}}(\mathbf{b} \mid \mathbf{a})$:

$$f_{\mathbf{y}}(\mathbf{y}_{k,l} \mid \boldsymbol{\theta}) = f_r(r_{k,l} \mid \boldsymbol{\theta})\, f_{\mathbf{s}}(\mathbf{s}_{k,l} \mid r_{k,l}, \boldsymbol{\theta}) = (2\pi\, \lambda_u)^{-½} \exp[-½\lambda_u^{-1}|r_{k,l} - d_{k,l}|^2] \qquad (4.5)$$
$$|2\pi\, \boldsymbol{\Lambda}|^{-½} \exp[-½\, (\mathbf{s}_{k,l} - \mathbf{h}_{k,l}\, r_{k,l})^{\dagger}\, \boldsymbol{\Lambda}^{-1}\, (\mathbf{s}_{k,l} - \mathbf{h}_{k,l}\, r_{k,l})]$$

Due to the assumption that the stochastic terms are white, $f_{\mathbf{y}}(\mathbf{y}|\boldsymbol{\theta})$ is the product of $f_{\mathbf{y}}(\mathbf{y}_{k,l}|\boldsymbol{\theta})$ over all possible combinations of k and l. Hence the likelihood of the complete data is:

$$L(\boldsymbol{\theta}) = \ln\{f_{\mathbf{y}}(\mathbf{y}|\boldsymbol{\theta})\} = \ln \prod_k \prod_l f_{\mathbf{y}}(\mathbf{y}_{k,l} \mid \boldsymbol{\theta}) = \sum_k \sum_l \ln\{ f_{\mathbf{y}}(\mathbf{y}_{k,l} \mid \boldsymbol{\theta})\} = \sum_k \sum_l L_{k,l}(\boldsymbol{\theta}) \qquad (4.6)$$

$$L_{k,l}(\boldsymbol{\theta}) = -{}^3\!/_2 \ln(2\pi) - {}^1\!/_2 \ln(\lambda_u \lambda_1 \lambda_2) - {}^1\!/_2 \lambda_u^{-1} |r_{k,l} - d_{k,l}|^2 -$$
$$- {}^1\!/_2\, (\mathbf{s}_{k,l} - \mathbf{h}_{k,l}\, r_{k,l})^{\dagger}\, \boldsymbol{\Lambda}^{-1}\, (\mathbf{s}_{k,l} - \mathbf{h}_{k,l}\, r_{k,l})$$

4.2.2 Expectation Step

After (4.6) is substituted for $\ln\{f_{\mathbf{y}}(\mathbf{y}|\boldsymbol{\theta})\}$ in equation (4.3), it follows that maximization of $Q(\boldsymbol{\theta}|\boldsymbol{\theta}^{[n]})$ is equivalent to minimization of:

$$J(\boldsymbol{\theta}|\boldsymbol{\theta}^{[n]}) = \sum_k \sum_l J_{k,l}(\boldsymbol{\theta} \mid \boldsymbol{\theta}^{[n]}) \qquad (4.7)$$

$$J_{k,l}(\boldsymbol{\theta}|\boldsymbol{\theta}^{[n]}) = \ln(\lambda_u \lambda_1 \lambda_2) + \lambda_u^{-1} |\, E[r_{k,l}|\mathbf{s},\boldsymbol{\theta}^{[n]}] - d_{k,l}\,|^2 +$$
$$+ (\mathbf{s}_{k,l} - \mathbf{h}_{k,l}\, E[r_{k,l}|\mathbf{s},\boldsymbol{\theta}^{[n]}])^{\dagger}\, \boldsymbol{\Lambda}^{-1}\, (\mathbf{s}_{k,l} - \mathbf{h}_{k,l}\, E[r_{k,l}|\mathbf{s},\boldsymbol{\theta}^{[n]}]) +$$
$$+ Var[r_{k,l}|\mathbf{s},\boldsymbol{\theta}^{[n]}]\, (\lambda_u^{-1} + \mathbf{h}_{k,l}^{\dagger}\, \boldsymbol{\Lambda}^{-1}\, \mathbf{h}_{k,l})$$

In order to find the conditional expectation and variance of $r_{k,l}$ given $\mathbf{s}$ and $\boldsymbol{\theta}^{[n]}$, we need to look at the conditional probability density:

$$f_r(r_{k,l} \mid \mathbf{s},\boldsymbol{\theta}^{[n]}) = f_{\mathbf{y}}(\mathbf{y}_{k,l} \mid \boldsymbol{\theta}^{[n]}) \,/\, f_{\mathbf{s}}(\mathbf{s}_{k,l} \mid \boldsymbol{\theta}^{[n]}) \qquad (4.8)$$

Substituting (4.1) for $f_{\mathbf{s}}(\mathbf{s}_{k,l} \mid \boldsymbol{\theta}^{[n]})$ and (4.5) for $f_{\mathbf{y}}(\mathbf{y}_{k,l} \mid \boldsymbol{\theta}^{[n]})$, it is not difficult to see that $f_r(r_{k,l} \mid \mathbf{s},\boldsymbol{\theta}^{[n]})$ is a Gaussian distribution with the following expression in its exponent:

$$-½\, \lambda_u^{-1}\, |r_{k,l} - d_{k,l}|^2 - ½\, (\mathbf{s}_{k,l} - \mathbf{h}_{k,l}\, r_{k,l})^{\dagger}\, \boldsymbol{\Lambda}^{-1}\, (\mathbf{s}_{k,l} - \mathbf{h}_{k,l}\, r_{k,l}) = \qquad (4.9)$$
$$= -½\, (r_{k,l}\, \mathbf{b}_{k,l} - \boldsymbol{\mu}_{k,l})^{\dagger}\, \boldsymbol{\Lambda}_r^{-1}\, (r_{k,l}\, \mathbf{b}_{k,l} - \boldsymbol{\mu}_{k,l})$$

where the following symbols are used:

$$\mathbf{b}_{k,l} = \begin{pmatrix} \mathbf{h}_{k,l} \\ 1 \end{pmatrix} \quad \boldsymbol{\mu}_{k,l} = \begin{pmatrix} \mathbf{s}_{k,l} \\ d_{k,l} \end{pmatrix} \quad \boldsymbol{\Lambda}_r = \begin{pmatrix} \boldsymbol{\Lambda} & \mathbf{0} \\ \mathbf{0} & \lambda_u \end{pmatrix} \qquad (4.10)$$

Thus, the conditional expectation is given by:

$$E[r_{k,l}|\mathbf{s},\boldsymbol{\theta}^{[n]}] = (\mathbf{b}_{k,l}^{\dagger}\, \boldsymbol{\Lambda}_r^{-1}\, \boldsymbol{\mu}_{k,l})\, (\mathbf{b}_{k,l}^{\dagger}\, \boldsymbol{\Lambda}_r^{-1}\, \mathbf{b}_{k,l})^{-1} = \qquad (4.11)$$
$$= \frac{\lambda_1^{-1}\mathbf{P}_1^{*}(\omega_x,\omega_z)\mathbf{S}_{\mathrm{V}}(\omega_x,\omega_z) + \lambda_2^{-1}\mathbf{P}_2^{*}(\omega_z,-\omega_x)\mathbf{S}_{\mathrm{H}}(\omega_x,\omega_z) + \lambda_u^{-1} d_{k,l}}{\lambda_1^{-1}\left|\mathbf{P}_1(\omega_x,\omega_z)\right|^2 + \lambda_2^{-1}\left|\mathbf{P}_2(\omega_z,-\omega_x)\right|^2 + \lambda_u^{-1}}$$

Note that this expression is identical to the vector Wiener filter [19]. For each of the parameters in equations (4.11) above and (4.12) below the current parameter estimate is substituted, though the superscript $^{[n]}$ is suppressed for brevity and clarity.

The conditional variance is given by:

$$Var[r_{k,l}|\mathbf{s},\boldsymbol{\theta}^{[n]}] = (\mathbf{b}_{k,l}{}^{\dagger}\ \boldsymbol{\Lambda}_r^{-1}\ \mathbf{b}_{k,l})^{-1} = \frac{1}{\lambda_1^{-1}\left|\mathbf{P}_1(\omega_x,\omega_z)\right|^2 + \lambda_2^{-1}\left|\mathbf{P}_2(\omega_z,-\omega_x)\right|^2 + \lambda_u^{-1}} \tag{4.12}$$

and the conditional expectation of $|r_{k,l}|^2$ is:

$$E[|r_{k,l}|^2|\mathbf{s},\boldsymbol{\theta}^{[n]}] = |\ E[r_{k,l}|\mathbf{s},\boldsymbol{\theta}^{[n]}]\ |^2 + Var[r_{k,l}|\mathbf{s},\boldsymbol{\theta}^{[n]}] \tag{4.13}$$

4.2.3 Minimization Step

Now, we take from equation (4.7) only the terms that involve $\mathbf{h}_{k,l}$:

$$J_{\mathbf{h}}(\boldsymbol{\theta}|\boldsymbol{\theta}^{[n]}) = \sum_k\sum_l \{\ Var[r_{k,l}|\mathbf{s},\boldsymbol{\theta}^{[n]}]\ \mathbf{h}_{k,l}{}^{\dagger}\ \boldsymbol{\Lambda}^{-1}\ \mathbf{h}_{k,l} + \\ + (\mathbf{s}_{k,l} - \mathbf{h}_{k,l}\ E[r_{k,l}|\mathbf{s},\boldsymbol{\theta}^{[n]}])^{\dagger}\ \boldsymbol{\Lambda}^{-1}\ (\mathbf{s}_{k,l} - \mathbf{h}_{k,l}\ E[r_{k,l}|\mathbf{s},\boldsymbol{\theta}^{[n]}])\ \} \tag{4.14}$$

Equation (4.14) can be written in terms of $\mathbf{P}_1$, $\mathbf{P}_2$, $\mathbf{S}_{\mathrm{V}}$ and $\mathbf{S}_{\mathrm{H}}$ explicitly:

$$J_{\mathbf{h}}(\boldsymbol{\theta}|\boldsymbol{\theta}^{[n]}) = \sum_k\sum_l \{\ Var[r_{k,l}|\mathbf{s},\boldsymbol{\theta}^{[n]}]\ \{\lambda_1^{-1}\ |\mathbf{P}_1(\omega_x,\ \omega_z)|^2 + \lambda_2^{-1}\ |\mathbf{P}_2(\omega_z,\ -\omega_x)|^2\} + \\ + \lambda_1^{-1}\ |\ \mathbf{S}_{\mathrm{V}}(\omega_x,\ \omega_z) - \mathbf{P}_1(\omega_x,\ \omega_z)\ E[r_{k,l}|\mathbf{s},\boldsymbol{\theta}^{[n]}]\ |^2 + \\ + \lambda_2^{-1}\ |\ \mathbf{S}_{\mathrm{H}}(\omega_x,\ \omega_z) - \mathbf{P}_2(\omega_z,\ -\omega_x)\ E[r_{k,l}|\mathbf{s},\boldsymbol{\theta}^{[n]}]\ |^2\ \} \tag{4.15}$$

The minimum of $J_{\mathbf{h}}(\boldsymbol{\theta}|\boldsymbol{\theta}^{[n]})$ is found through zeroing the following $2\mathrm{N}_{\mathrm{DFT}}{}^2$ derivatives:

$$\frac{\partial J_{\mathbf{h}}}{\partial \mathbf{P}_1{}^{*}(\omega_x,\omega_z)} = 2\lambda_1^{-1}\ \{\ \mathbf{P}_1(\omega_x,\ \omega_z)\ \{Var[\mathbf{R}(\omega_x,\ \omega_z)|\mathbf{s},\boldsymbol{\theta}^{[n]}] + |\ E[\mathbf{R}(\omega_x,\ \omega_z)|\mathbf{s},\boldsymbol{\theta}^{[n]}]\ |^2\} - \\ - E[\mathbf{R}(\omega_x,\ \omega_z)|\mathbf{s},\boldsymbol{\theta}^{[n]}]^{*}\ \mathbf{S}_{\mathrm{V}}(\omega_x,\ \omega_z)\ \} \tag{4.16}$$

$$\frac{\partial J_{\mathbf{h}}}{\partial \mathbf{P}_2{}^{*}(\omega_x,\omega_z)} = 2\lambda_2^{-1}\ \{\ \mathbf{P}_2(\omega_x,\ \omega_z)\ \{Var[\mathbf{R}(-\omega_z,\omega_x)|\mathbf{s},\boldsymbol{\theta}^{[n]}] + |\ E[\mathbf{R}(-\omega_z,\omega_x)|\mathbf{s},\boldsymbol{\theta}^{[n]}]\ |^2\} - \\ - E[\mathbf{R}(-\omega_z,\omega_x)|\mathbf{s},\boldsymbol{\theta}^{[n]}]^{*}\ \mathbf{S}_{\mathrm{H}}(-\omega_z,\omega_x)\ \}$$

Thus the update of the estimates of the system responses is:

$$\mathbf{P}_1{}^{[n+1]}(\omega_x,\ \omega_z) = \frac{E[\mathbf{R}(\omega_x,\omega_z)\ |\ \mathbf{s},\boldsymbol{\theta}^{[n]}]^{*}\ \mathbf{S}_{\mathrm{V}}(\omega_x,\omega_z)}{E[\left|\mathbf{R}(\omega_x,\omega_z)\right|^2\ |\ \mathbf{s},\boldsymbol{\theta}^{[n]}]} \tag{4.17}$$

$$\mathbf{P}_2{}^{[n+1]}(\omega_x,\ \omega_z) = \frac{E[\mathbf{R}(-\omega_z,\omega_x)\ |\ \mathbf{s},\boldsymbol{\theta}^{[n]}]^{*}\ \mathbf{S}_{\mathrm{H}}(-\omega_z,\omega_x)}{E[\left|\mathbf{R}(-\omega_z,\omega_x)\right|^2\ |\ \mathbf{s},\boldsymbol{\theta}^{[n]}]}$$

Next, we take from equation (4.7) only terms related to $\boldsymbol{\Lambda}$:

$$J_{\boldsymbol{\Lambda}}(\boldsymbol{\theta}|\boldsymbol{\theta}^{[n]}) = \sum_k\sum_l \ln(\lambda_1\lambda_2) + J_{\mathbf{h}}(\boldsymbol{\theta}|\boldsymbol{\theta}^{[n]}) \tag{4.18}$$

Substituting (4.15) for $J_{\mathbf{h}}(\boldsymbol{\theta}|\boldsymbol{\theta}^{[n]})$ and (4.17) for $\mathbf{P}_1$ and $\mathbf{P}_2$, and noting that the minimum of $f(\lambda)=\ln\lambda+\lambda^{-1}g$ is at $\lambda=g$, the values of λ_1 and λ_2 that minimize $J_{\boldsymbol{\Lambda}}(\boldsymbol{\theta}|\boldsymbol{\theta}^{[n]})$ are:

$$\lambda_1^{[n+1]} = N_{DFT}^{-2} \sum_k \sum_l \{ Var[r_{k,l}|\mathbf{s},\boldsymbol{\theta}^{[n]}] \, |\mathbf{P}_1^{[n+1]}(\omega_x, \omega_z)|^2 + \\ + | \mathbf{S}_V(\omega_x, \omega_z) - \mathbf{P}_1^{[n+1]}(\omega_x, \omega_z) \, E[r_{k,l}|\mathbf{s},\boldsymbol{\theta}^{[n]}] \, |^2 \} \tag{4.19}$$

$$\lambda_2^{[n+1]} = N_{DFT}^{-2} \sum_k \sum_l \{ Var[r_{k,l}|\mathbf{s},\boldsymbol{\theta}^{[n]}] \, |\mathbf{P}_2^{[n+1]}(\omega_z, -\omega_x)|^2 + \\ + | \mathbf{S}_H(\omega_x, \omega_z) - \mathbf{P}_2^{[n+1]}(\omega_z, -\omega_x) \, E[r_{k,l}|\mathbf{s},\boldsymbol{\theta}^{[n]}] \, |^2 \}$$

Then, we take from equation (4.7) only the terms that depend on $d_{k,l}$:

$$J_d(\boldsymbol{\theta}|\boldsymbol{\theta}^{[n]}) = \lambda_u^{-1} \sum_k \sum_l | \, E[r_{k,l}|\mathbf{s},\boldsymbol{\theta}^{[n]}] - d_{k,l} \, |^2 \tag{4.20}$$

It is simple to see that the value of $d_{k,l}$ that minimizes $J_d(\boldsymbol{\theta}|\boldsymbol{\theta}^{[n]})$ is:

$$d_{k,l}^{[n+1]} = E[r_{k,l}|\mathbf{s},\boldsymbol{\theta}^{[n]}] \tag{4.21}$$

Finally, we substitute (4.21) for $d_{k,l}$ in (4.7) then take only the terms that depend on λ_u:

$$J_u(\boldsymbol{\theta}|\boldsymbol{\theta}^{[n]}) = \sum_k \sum_l \ln(\lambda_u) + \lambda_u^{-1} \, Var[r_{k,l}|\mathbf{s},\boldsymbol{\theta}^{[n]}] \tag{4.22}$$

The minimum of $J_u(\boldsymbol{\theta}|\boldsymbol{\theta}^{[n]})$ is achieved when the value of λ_u is:

$$\lambda_u^{[n+1]} = N_{DFT}^{-2} \sum_k \sum_l Var \, [r_{k,l}|\mathbf{s},\boldsymbol{\theta}^{[n]}] \tag{4.23}$$

4.2.4 Special Cases

Same Noise Variance in Both Views

If we assume that the noise variance is the same in both RF images $\lambda_1 = \lambda_2 = \lambda$, then the only change in the above EM algorithm is that the average of the 2 expressions in (4.19) should be used to update the variance $\lambda^{[n+1]}$:

$$\lambda^{[n+1]} = \tfrac{1}{2} N_{DFT}^{-2} \sum_k \sum_l \{ Var[r_{k,l}|\mathbf{s},\boldsymbol{\theta}^{[n]}] \, \{|\mathbf{P}_1^{[n+1]}(\omega_x, \omega_z)|^2 + |\mathbf{P}_2^{[n+1]}(\omega_z, -\omega_x)|^2\} + \\ + | \mathbf{S}_V(\omega_x, \omega_z) - \mathbf{P}_1^{[n+1]}(\omega_x, \omega_z) \, E[r_{k,l}|\mathbf{s},\boldsymbol{\theta}^{[n]}] \, |^2 + \\ + | \mathbf{S}_H(\omega_x, \omega_z) - \mathbf{P}_2^{[n+1]}(\omega_z, -\omega_x) \, E[r_{k,l}|\mathbf{s},\boldsymbol{\theta}^{[n]}] \, |^2 \} \tag{4.24}$$

This is a straightforward result when λ_1 and λ_2 are replaced by λ in equations (4.15) and (4.18).

Same Blur in Both Views

If we assume identical system response in both scans $\mathbf{P}_1 = \mathbf{P}_2 = \mathbf{P}$, then the minimum of $J_{\mathbf{h}}(\boldsymbol{\theta}|\boldsymbol{\theta}^{[n]})$ in (4.15) is found through zeroing the following N_{DFT}^2 derivatives:

$$\frac{\partial J_{\mathbf{h}}}{\partial \mathbf{P}^*(\omega_x, \omega_z)} = 2 \{ \lambda_1^{-1} \mathbf{P}(\omega_x, \omega_z) \, E[\, |r_{k,l}|^2 \, |\mathbf{s},\boldsymbol{\theta}^{[n]}] + \lambda_2^{-1} \mathbf{P}(\omega_x, \omega_z) \, E[\, |r_{-l,k}|^2 \, |\mathbf{s},\boldsymbol{\theta}^{[n]}] + \\ - \lambda_1^{-1} E[r_{k,l} \, |\mathbf{s},\boldsymbol{\theta}^{[n]}]^* \, \mathbf{S}_V(\omega_x, \omega_z) - \lambda_2^{-1} E[r_{-l,k} \, |\mathbf{s},\boldsymbol{\theta}^{[n]}]^* \, \mathbf{S}_H(-\omega_z, \omega_x) \} \tag{4.25}$$

Thus the update of the estimate of the system response becomes:

$$\mathbf{P}^{[n+1]}(\omega_x, \omega_z) = \\ = \frac{\lambda_1^{-1} E[\mathbf{R}(\omega_x, \omega_z) \, | \, \mathbf{s}, \boldsymbol{\theta}^{[n]}]^* \, \mathbf{S}_V(\omega_x, \omega_z) + \lambda_2^{-1} E[\mathbf{R}(-\omega_z, \omega_x) \, | \, \mathbf{s}, \boldsymbol{\theta}^{[n]}]^* \, \mathbf{S}_H(-\omega_z, \omega_x)}{\lambda_1^{-1} E[|\mathbf{R}(\omega_x, \omega_z)|^2 \, | \, \mathbf{s}, \boldsymbol{\theta}^{[n]}] + \lambda_2^{-1} E[|\mathbf{R}(-\omega_z, \omega_x)|^2 \, | \, \mathbf{s}, \boldsymbol{\theta}^{[n]}]} \tag{4.26}$$

4.2.5 Initialization and Constraints

Initialization

Being highly non-linear the likelihood function $L(\boldsymbol{\theta})$ has multiple maxima, and therefore the initial conditions $\boldsymbol{\theta}^{[0]}$ have a great effect on the ability of the EM algorithm to converge to a good estimation. We found that $\mathbf{P}_1^{[0]}$ and $\mathbf{P}_2^{[0]}$ should have the same value at all frequencies, that is they should be the DFT of an impulse at the origin. The initialization for $d^{[0]}$ should be the average of the RF images $\mathbf{S}_V$ and $\mathbf{S}_H$. The rationale for this appears in equation (4.11) when a constant value is substituted for the blur. For the noise variance the initial estimate is higher than the true value, as it was found in [21] to produce better results.

Iterations

In each iteration of the algorithm the E-step is followed by the M-step:

1. The E-step consists of the evaluation of the expressions in (4.11), (4.12) and (4.13), namely the expectation and variance of $\mathbf{R}(\omega_x, \omega_z)$ are calculated using the estimated values of the parameters from the previous M-step.
2. The M-step consists of the evaluation of the expressions in (4.17) (or alternatively(4.26)), (4.19) (or alternatively (4.24)), (4.21) and (4.23), namely a new estimate of the parameters is calculated using the expectation and variance of $\mathbf{R}(\omega_x, \omega_z)$ from the previous E-step.

These 2 steps can be performed in succession for a pre-defined number of iterations or until the change in $\mathbf{P}_1$ and $\mathbf{P}_2$ is small enough with respect to some distance measure.

Scaling

Since the system response and the tissue reflectivity are coupled through multiplication, the scaling of their estimations can drift in inverse directions. In order to avoid divergence, arbitrary scaling must be enforced every iteration, and we chose to normalize the PSF of the blur after it is estimated in the M-step to have a unit total power. In the frequency domain this translates into $\|\mathbf{P}_1^{[n+1]}\|^2 = \|\mathbf{P}_2^{[n+1]}\|^2 = N_{DFT}^2$.

Limiting the Noise-to-Speckle Ratio

In the initial iterations the estimation of the variances λ_1, λ_2 and λ_u is unreliable. As a result the estimation in (4.11) and (4.12) is much improved if λ_u is limited such that λ_1/λ_u and λ_2/λ_u are not too large or small relatively to $\max|\mathbf{P}_1(\omega_x, \omega_z)|^2$ and $\max|\mathbf{P}_2(\omega_x, \omega_z)|^2$ respectively.

Windowing In the Space Domain

Given that equation (3.13) requires zero-padding in the space domain, the estimated tissue reflectivity and blur PSF's can be multiplied by limiting window functions $\boldsymbol{\Omega}_{\mathbf{R}}(x, z)$, $\boldsymbol{\Omega}_{\mathbf{P1}}(x, z)$ and $\boldsymbol{\Omega}_{\mathbf{P2}}(x, z)$ respectively to suppress unwanted non-zero values. This requires an inverse Fourier-transform of the reflectivity and/or system responses prior to windowing and a Fourier-transform afterwards every prescribed number of iterations. For example, if the same blur is assumed in both scans, the estimation in (4.26) can be modified as follows:

$$\mathbf{P}^{[n+1]}(\omega_x, \omega_z) = \mathrm{DFT}\{\ \mathrm{IDFT}\{\ \mathbf{P}^{[n+1]}(\omega_x, \omega_z)\ \}\ \boldsymbol{\Omega}_{\mathbf{P}}^{[n+1]}(x, z)\ \} \tag{4.27}$$

The windowing can be hard, i.e. rectangular, or utilize soft limit, e.g. raised-cosine, and can change during the iterations. Note that space-domain windowing is equivalent to averaging in the frequency domain between estimates at neighbouring frequncies.

Windowing In the Frequency Domain

Prior knowledge about the system response can be utilized in order to reduce the sensitivity of the estimation to noise. The estimated frequency response of the system can be multiplied by a window function $\mathbf{W}(\omega_x, \omega_z)$ to suppress out-of-band frequencies that undoubtedly result from noise. For example, if the same system response is assumed in both views, the estimation in equation (4.26) can be modified as follows:

$$\mathbf{P}^{[n+1]}(\omega_x, \omega_z) = \mathbf{P}^{[n+1]}(\omega_x, \omega_z)\, \mathbf{W}^{[n+1]}(\omega_x, \omega_z) \;, \qquad \forall \omega_x,\omega_z \;\; 0 \le \mathbf{W}^{[n+1]}(\omega_x, \omega_z) \le 1 \qquad (4.28)$$

For example, if $\mathbf{W}^{[n+1]}(\omega_x, \omega_z)$ is separable: $\mathbf{W}^{[n+1]}(\omega_x, \omega_z) = \mathbf{W}_1{}^{[n+1]}(\omega_x)\, \mathbf{W}_2{}^{[n+1]}(\omega_z)$, the window functions $\mathbf{W}_{1,2}(\omega)$ can be raised-cosine, Hamming or Blackman windows centered around the system's expected peak frequency. The last 2 constraints can be combined, such that windowing is performed first in the space domain then in the frequency domain or vice versa.

4.3 EM with the Blur as the Hidden Data

4.3.1 The Complete Data

A different definition of the complete data for the problem at hand is possible by taking the system response $\mathbf{h}_{k,l}$ to be the *hidden data*: $\mathbf{y}_{k,l} = \begin{pmatrix} \mathbf{s}_{k,l} \\ \mathbf{h}_{k,l} \end{pmatrix} = \begin{pmatrix} \mathbf{S}_{\mathrm{V}}(\omega_x,\omega_z) \\ \mathbf{S}_{\mathrm{H}}(\omega_x,\omega_z) \\ \mathbf{P}_1(\omega_x,\omega_z) \\ \mathbf{P}_2(\omega_z,-\omega_x) \end{pmatrix}$, so the non-invertible mapping is: $\mathbf{s}_{k,l} = (\, \mathbf{I} \;\; \mathbf{0} \,)\, \mathbf{y}_{k,l} = \begin{pmatrix} 1 & 0 & 0 & 0 \\ 0 & 1 & 0 & 0 \end{pmatrix} \begin{pmatrix} \mathbf{S}_{\mathrm{V}}(\omega_x,\omega_z) \\ \mathbf{S}_{\mathrm{H}}(\omega_x,\omega_z) \\ \mathbf{P}_1(\omega_x,\omega_z) \\ \mathbf{P}_2(\omega_z,-\omega_x) \end{pmatrix}$.

Therefore, in this section 4.3, the reflectivity image is treated as deterministic, while the response $\mathbf{h}_{k,l}$ is considered as stochastic with mean $\boldsymbol{\eta}_{k,l}$ and a diagonal 2×2 covariance matrix $\boldsymbol{\Lambda}_{\mathbf{h}}$, where the diagonal elements are the variances $\lambda_{\mathbf{P}1}$ and $\lambda_{\mathbf{P}2}$ of $\mathbf{P}_1(\omega_x, \omega_z)$ and $\mathbf{P}_2(\omega_x, \omega_z)$ respectively. This approach does not conform to the model in section 3.2, but nevertheless it produces results with similar quality as those produced by the approach of the reflectivity image as the hidden data. Now, the reflectivity image is the estimation target as part of the parameter set $\boldsymbol{\theta}_{k,l} \equiv [\boldsymbol{\eta}_{k,l}{}^{\mathrm{T}}, \lambda_{\mathbf{P}1}, \lambda_{\mathbf{P}2}, r_{k,l}, \lambda_1, \lambda_2]^{\mathrm{T}}$.

According to the conditional-probability formula:

$$f_{\mathbf{y}}(\mathbf{y}_{k,l} \mid \boldsymbol{\theta}) = f_r(\mathbf{h}_{k,l} \mid \boldsymbol{\theta})\, f_{\mathbf{s}}(\mathbf{s}_{k,l} \mid \mathbf{h}_{k,l}, \boldsymbol{\theta}) = |2\pi\, \boldsymbol{\Lambda}_{\mathbf{h}}|^{-\frac{1}{2}} \exp[-\tfrac{1}{2}(\mathbf{h}_{k,l} - \boldsymbol{\eta}_{k,l})^{\dagger}\, \boldsymbol{\Lambda}_{\mathbf{h}}^{-1}\, (\mathbf{h}_{k,l} - \boldsymbol{\eta}_{k,l})] \qquad (4.29)$$
$$|2\pi\, \boldsymbol{\Lambda}|^{-\frac{1}{2}} \exp[-\tfrac{1}{2}\, (\mathbf{s}_{k,l} - \mathbf{h}_{k,l}\, r_{k,l})^{\dagger}\, \boldsymbol{\Lambda}^{-1}\, (\mathbf{s}_{k,l} - \mathbf{h}_{k,l}\, r_{k,l})]$$

Due to the assumption that the stochastic terms are white, $f_{\mathbf{y}}(\mathbf{y}|\boldsymbol{\theta})$ is the product of $f_{\mathbf{y}}(\mathbf{y}_{k,l}|\boldsymbol{\theta})$ over all possible combinations of k and l. Hence the likelihood of the complete data is:

$$L(\boldsymbol{\theta}) = \ln\{f_{\mathbf{y}}(\mathbf{y}|\boldsymbol{\theta})\} = \ln \prod_k \prod_l f_{\mathbf{y}}(\mathbf{y}_{k,l} \mid \boldsymbol{\theta}) = \sum_k \sum_l \ln\{ f_{\mathbf{y}}(\mathbf{y}_{k,l} \mid \boldsymbol{\theta})\} = \sum_k \sum_l L_{k,l}(\boldsymbol{\theta}) \qquad (4.30)$$

$$L_{k,l}(\boldsymbol{\theta}) = -2\, \ln(2\pi) - \tfrac{1}{2}\, \ln(\lambda_{\mathbf{P}1}\lambda_{\mathbf{P}2}\lambda_1\lambda_2) - \tfrac{1}{2}(\mathbf{h}_{k,l} - \boldsymbol{\eta}_{k,l})^{\dagger}\, \boldsymbol{\Lambda}_{\mathbf{h}}^{-1}\, (\mathbf{h}_{k,l} - \boldsymbol{\eta}_{k,l}) -$$
$$- \tfrac{1}{2}\, (\mathbf{s}_{k,l} - \mathbf{h}_{k,l}\, r_{k,l})^{\dagger}\, \boldsymbol{\Lambda}^{-1}\, (\mathbf{s}_{k,l} - \mathbf{h}_{k,l}\, r_{k,l})$$

4.3.2 Expectation Step

After (4.30) is substituted for $\ln\{f_{\mathbf{y}}(\mathbf{y}|\boldsymbol{\theta})\}$ in equation (4.3), it follows that maximization of $Q(\boldsymbol{\theta}|\boldsymbol{\theta}^{[n]})$ is equivalent to minimization of:

$$J(\boldsymbol{\theta}|\boldsymbol{\theta}^{[n]}) = \sum_k \sum_l J_{k,l}(\boldsymbol{\theta} \mid \boldsymbol{\theta}^{[n]}) \tag{4.31}$$

$$\begin{aligned} J_{k,l}(\boldsymbol{\theta}|\boldsymbol{\theta}^{[n]}) = \ln(\lambda_{\mathbf{P}1}\lambda_{\mathbf{P}2}\lambda_1\lambda_2) &+ (E[\mathbf{h}_{k,l}|\mathbf{s},\boldsymbol{\theta}^{[n]}] - \boldsymbol{\eta}_{k,l})^{\dagger}\, \boldsymbol{\Lambda}_{\mathbf{h}}^{-1}\, (E[\mathbf{h}_{k,l}|\mathbf{s},\boldsymbol{\theta}^{[n]}] - \boldsymbol{\eta}_{k,l}) + \\ &+ (\mathbf{s}_{k,l} - E[\mathbf{h}_{k,l}|\mathbf{s},\boldsymbol{\theta}^{[n]}]\, r_{k,l})^{\dagger}\, \boldsymbol{\Lambda}^{-1}\, (\mathbf{s}_{k,l} - E[\mathbf{h}_{k,l}|\mathbf{s},\boldsymbol{\theta}^{[n]}]\, r_{k,l}) + \\ &+ \mathrm{tr}\{(\boldsymbol{\Lambda}_{\mathbf{h}}^{-1} + |r_{k,l}|^2\, \boldsymbol{\Lambda}^{-1})\, \mathit{Covar}[\mathbf{h}_{k,l}|\mathbf{s},\boldsymbol{\theta}^{[n]}]\} \end{aligned}$$

In the above derivation we used the identity

$$\mathbf{v}^{\dagger}\, \mathbf{A}\, \mathbf{w} = \mathrm{tr}(\mathbf{A}\, \mathbf{w}\, \mathbf{v}^{\dagger}) \tag{4.32}$$

where $\mathbf{A}$ is a $N \times N$ matrix, $\mathbf{v}$ and $\mathbf{w}$ are $N \times 1$ vectors, and $\mathrm{tr}(\mathbf{A})$ denotes the trace of $\mathbf{A}$.

Following steps similar to those in section 4.2.2, we find that the conditional expectation of $\mathbf{h}_{k,l}$ given $\mathbf{s}$ and $\boldsymbol{\theta}^{[n]}$ is given by:

$$E[\mathbf{P}_1(\omega_x, \omega_z)|\mathbf{s},\boldsymbol{\theta}^{[n]}] = \frac{\lambda_1^{-1}\mathbf{R}(\omega_x,\omega_z)^{*}\mathbf{S}_{\mathrm{V}}(\omega_x,\omega_z) + \lambda_{\mathbf{P}1}^{-1}\eta_{\mathbf{P}1k,l}}{\lambda_1^{-1}\left|\mathbf{R}(\omega_x,\omega_z)\right|^2 + \lambda_{\mathbf{P}1}^{-1}} \tag{4.33}$$

$$E[\mathbf{P}_2(\omega_z, -\omega_x)|\mathbf{s},\boldsymbol{\theta}^{[n]}] = \frac{\lambda_2^{-1}\mathbf{R}(\omega_x,\omega_z)^{*}\mathbf{S}_{\mathrm{H}}(\omega_x,\omega_z) + \lambda_{\mathbf{P}2}^{-1}\eta_{\mathbf{P}2l,-k}}{\lambda_2^{-1}\left|\mathbf{R}(\omega_x,\omega_z)\right|^2 + \lambda_{\mathbf{P}2}^{-1}}$$

$$\Downarrow$$

$$E[\mathbf{P}_2(\omega_x, \omega_z)|\mathbf{s},\boldsymbol{\theta}^{[n]}] = \frac{\lambda_2^{-1}\mathbf{R}(-\omega_z,\omega_x)^{*}\mathbf{S}_{\mathrm{H}}(-\omega_z,\omega_x) + \lambda_{\mathbf{P}2}^{-1}\eta_{\mathbf{P}2k,l}}{\lambda_2^{-1}\left|\mathbf{R}(-\omega_z,\omega_x)\right|^2 + \lambda_{\mathbf{P}2}^{-1}}$$

For each of the parameters in equations (4.33) above and (4.34) below the current parameter estimate is substituted, though the superscript $^{[n]}$ is suppressed for brevity and clarity.

The conditional variance is given by:

$$Var[\mathbf{P}_1(\omega_x, \omega_z)|\mathbf{s},\boldsymbol{\theta}^{[n]}] = (\mathbf{b}_{\mathrm{V}k,l}^{\dagger}\, \boldsymbol{\Lambda}_{\mathrm{P}1}^{-1}\, \mathbf{b}_{\mathrm{V}k,l})^{-1} = \frac{1}{\lambda_1^{-1}\left|\mathbf{R}(\omega_x,\omega_z)\right|^2 + \lambda_{\mathbf{P}1}^{-1}} \tag{4.34}$$

$$Var[\mathbf{P}_2(\omega_x, \omega_z)|\mathbf{s},\boldsymbol{\theta}^{[n]}] = (\mathbf{b}_{\mathrm{H}\text{-}l,k}^{\dagger}\, \boldsymbol{\Lambda}_{\mathrm{P}2}^{-1}\, \mathbf{b}_{\mathrm{H}\text{-}l,k})^{-1} = \frac{1}{\lambda_2^{-1}\left|\mathbf{R}(-\omega_z,\omega_x)\right|^2 + \lambda_{\mathbf{P}2}^{-1}}$$

and the conditional expectation of $|\mathbf{P}_1(\omega_x, \omega_z)|^2$ and $|\mathbf{P}_2(\omega_x, \omega_z)|^2$ is:

$$\begin{aligned} E[|\mathbf{P}_1(\omega_x, \omega_z)|^2|\mathbf{s},\boldsymbol{\theta}^{[n]}] &= |\, E[\mathbf{P}_1(\omega_x, \omega_z)|\mathbf{s},\boldsymbol{\theta}^{[n]}]\, |^2 + Var[\mathbf{P}_1(\omega_x, \omega_z)|\mathbf{s},\boldsymbol{\theta}^{[n]}] \\ E[|\mathbf{P}_2(\omega_x, \omega_z)|^2|\mathbf{s},\boldsymbol{\theta}^{[n]}] &= |\, E[\mathbf{P}_2(\omega_x, \omega_z)|\mathbf{s},\boldsymbol{\theta}^{[n]}]\, |^2 + Var[\mathbf{P}_2(\omega_x, \omega_z)|\mathbf{s},\boldsymbol{\theta}^{[n]}] \end{aligned} \tag{4.35}$$

4.3.3 Minimization Step

Now, we take from equation (4.31) only the terms that involve $r_{k,l}$ and use the identity of (4.32):

$$J_r(\boldsymbol{\theta}|\boldsymbol{\theta}^{[n]}) = \sum_k \sum_l \{ |r_{k,l}|^2 \, \mathrm{tr}\{\boldsymbol{\Lambda}^{-1} \, Covar[\mathbf{h}_{k,l}|\mathbf{s},\boldsymbol{\theta}^{[n]}]\} + \\ + (\mathbf{s}_{k,l} - E[\mathbf{h}_{k,l}|\mathbf{s},\boldsymbol{\theta}^{[n]}] \, r_{k,l})^{\dagger} \, \boldsymbol{\Lambda}^{-1} \, (\mathbf{s}_{k,l} - E[\mathbf{h}_{k,l}|\mathbf{s},\boldsymbol{\theta}^{[n]}] \, r_{k,l}) \, \} \tag{4.36}$$

Equation (4.36) can be written in terms of $\mathbf{R}$, $\mathbf{S}_V$ and $\mathbf{S}_H$ explicitly:

$$J_r(\boldsymbol{\theta}|\boldsymbol{\theta}^{[n]}) = \sum_k \sum_l \{ |\mathbf{R}(\omega_x, \omega_z)|^2 \, \{\lambda_1^{-1} \, Var[\mathbf{P}_1(\omega_x, \omega_z)|\mathbf{s},\boldsymbol{\theta}^{[n]}] + \lambda_2^{-1} \, Var[\mathbf{P}_2(\omega_z, -\omega_x)|\mathbf{s},\boldsymbol{\theta}^{[n]}]\} + \\ + \lambda_1^{-1} \, | \, \mathbf{S}_V(\omega_x, \omega_z) - E[\mathbf{P}_1(\omega_x, \omega_z)|\mathbf{s},\boldsymbol{\theta}^{[n]}] \, \mathbf{R}(\omega_x, \omega_z) \, |^2 + \\ + \lambda_2^{-1} \, | \, \mathbf{S}_H(\omega_x, \omega_z) - E[\mathbf{P}_2(\omega_z, -\omega_x)|\mathbf{s},\boldsymbol{\theta}^{[n]}] \, \mathbf{R}(\omega_x, \omega_z) \, |^2 \, \} \tag{4.37}$$

Minimization of $J_r(\boldsymbol{\theta}|\boldsymbol{\theta}^{[n]})$ yields the update of the estimate of the reflectivity image is:

$$\mathbf{R}^{[n+1]}(\omega_x, \omega_z) = \\ = \frac{\lambda_1^{-1} E[\mathbf{P}_1(\omega_x,\omega_z) \,|\, \mathbf{s},\boldsymbol{\theta}^{[n]}]^* \, \mathbf{S}_V(\omega_x,\omega_z) + \lambda_2^{-1} E[\mathbf{P}_2(\omega_z,-\omega_x) \,|\, \mathbf{s},\boldsymbol{\theta}^{[n]}]^* \, \mathbf{S}_H(\omega_x,\omega_z)}{\lambda_1^{-1} E[|\mathbf{P}_1(\omega_x,\omega_z)|^2 \,|\, \mathbf{s},\boldsymbol{\theta}^{[n]}] + \lambda_2^{-1} E[|\mathbf{P}_2(\omega_z,-\omega_x)|^2 \,|\, \mathbf{s},\boldsymbol{\theta}^{[n]}]} \tag{4.38}$$

Next, we take from equation (4.31) only terms related to $\boldsymbol{\Lambda}$ to construct $J_{\boldsymbol{\Lambda}}(\boldsymbol{\theta}|\boldsymbol{\theta}^{[n]})$, and the values of λ_1 and λ_2 that minimize $J_{\boldsymbol{\Lambda}}(\boldsymbol{\theta}|\boldsymbol{\theta}^{[n]})$ are:

$$\lambda_1^{[n+1]} = \mathrm{N_{DFT}}^{-2} \sum_k \sum_l \{ |\mathbf{R}^{[n+1]}(\omega_x, \omega_z)|^2 \, Var[\mathbf{P}_1(\omega_x, \omega_z)|\mathbf{s},\boldsymbol{\theta}^{[n]}] + \\ + | \, \mathbf{S}_V(\omega_x, \omega_z) - E[\mathbf{P}_1(\omega_x, \omega_z)|\mathbf{s},\boldsymbol{\theta}^{[n]}] \, \mathbf{R}^{[n+1]}(\omega_x, \omega_z) \, |^2 \, \} \tag{4.39}$$

$$\lambda_2^{[n+1]} = \mathrm{N_{DFT}}^{-2} \sum_k \sum_l \{ |\mathbf{R}^{[n+1]}(\omega_x, \omega_z)|^2 \, Var[\mathbf{P}_2(\omega_z, -\omega_x)|\mathbf{s},\boldsymbol{\theta}^{[n]}] + \\ + | \, \mathbf{S}_H(\omega_x, \omega_z) - E[\mathbf{P}_2(\omega_z, -\omega_x)|\mathbf{s},\boldsymbol{\theta}^{[n]}] \, \mathbf{R}^{[n+1]}(\omega_x, \omega_z) \, |^2 \, \}$$

Then, we compose $J_{\boldsymbol{\eta}}(\boldsymbol{\theta}|\boldsymbol{\theta}^{[n]})$ from the terms that depend only on $\boldsymbol{\eta}_{k,l}$ in equation (4.31), and the value of $\boldsymbol{\eta}_{k,l}$ that minimizes $J_{\boldsymbol{\eta}}(\boldsymbol{\theta}|\boldsymbol{\theta}^{[n]})$ is:

$$\boldsymbol{\eta}_{k,l}^{[n+1]} = E[\mathbf{h}_{k,l}|\mathbf{s},\boldsymbol{\theta}^{[n]}] \tag{4.40}$$

Finally, we substitute (4.40) for $\boldsymbol{\eta}_{k,l}$ in (4.31) then take only terms involving $\lambda_{\mathbf{P}1}$ and $\lambda_{\mathbf{P}2}$ to form $J_{\boldsymbol{\Lambda}\mathbf{h}}(\boldsymbol{\theta}|\boldsymbol{\theta}^{[n]})$, and its minimum is achieved when the values of $\lambda_{\mathbf{P}1}$ and $\lambda_{\mathbf{P}2}$ are:

$$\lambda_{\mathbf{P}1}^{[n+1]} = \mathrm{N_{DFT}}^{-2} \sum_k \sum_l Var \, [\mathbf{P}_1(\omega_x, \omega_z)|\mathbf{s},\boldsymbol{\theta}^{[n]}] \\ \lambda_{\mathbf{P}2}^{[n+1]} = \mathrm{N_{DFT}}^{-2} \sum_k \sum_l Var \, [\mathbf{P}_2(\omega_z, \omega_x)|\mathbf{s},\boldsymbol{\theta}^{[n]}] \tag{4.41}$$

4.3.4 Special Cases

Same Noise Variance in Both Views

If we assume that the noise variance is the same in both RF images $\lambda_1 = \lambda_2 = \lambda$, then the only change in the above EM algorithm is that the average of the 2 expressions in (4.39) should be used to update the variance $\lambda^{[n+1]}$:

$$\lambda^{[n+1]} = \tfrac{1}{2}\, N_{DFT}^{-2} \sum_k \sum_l \{\, |\mathbf{R}^{[n+1]}(\omega_x,\omega_z)|^2 \, \{Var[\mathbf{P}_1(\omega_x,\omega_z)|\mathbf{s},\boldsymbol{\theta}^{[n]}] + Var[\mathbf{P}_2(\omega_z,-\omega_x)|\mathbf{s},\boldsymbol{\theta}^{[n]}]\} + \quad (4.42)$$

$$+ |\, \mathbf{S}_V(\omega_x,\, \omega_z) - E[\mathbf{P}_1(\omega_x,\, \omega_z)|\mathbf{s},\boldsymbol{\theta}^{[n]}]\, \mathbf{R}^{[n+1]}(\omega_x,\, \omega_z)\, |^2 +$$

$$+ |\, \mathbf{S}_H(\omega_x,\, \omega_z) - E[\mathbf{P}_2(\omega_z,\, -\omega_x)|\mathbf{s},\boldsymbol{\theta}^{[n]}]\, \mathbf{R}^{[n+1]}(\omega_x,\, \omega_z)\, |^2 \,\}$$

This is a straightforward result when λ_1 and λ_2 are replaced by λ in $J_{\boldsymbol{\Lambda}}(\boldsymbol{\theta}|\boldsymbol{\theta}^{[n]})$.

Same Blur in Both Views

If we assume identical system response in both scans $\mathbf{P}_1 = \mathbf{P}_2 = \mathbf{P}$, then the conditional expectation and variance of $\mathbf{P}$ are:

$$E[\mathbf{P}(\omega_x,\, \omega_z)|\mathbf{s},\boldsymbol{\theta}^{[n]}] = \quad (4.43)$$

$$= \frac{\lambda_1^{-1}\mathbf{R}(\omega_x,\omega_z)^*\mathbf{S}_V(\omega_x,\omega_z) + \lambda_2^{-1}\mathbf{R}(-\omega_z,\omega_x)^*\mathbf{S}_H(-\omega_z,\omega_x) + \lambda_{\mathbf{P}}^{-1}\eta_{\mathbf{P}k,l}}{\lambda_1^{-1}\left|\mathbf{R}(\omega_x,\omega_z)\right|^2 + \lambda_2^{-1}\left|\mathbf{R}(-\omega_z,\omega_x)\right|^2 + \lambda_{\mathbf{P}}^{-1}}$$

$$Var[\mathbf{P}(\omega_x,\, \omega_z)|\mathbf{s},\boldsymbol{\theta}^{[n]}] = \frac{1}{\lambda_1^{-1}\left|\mathbf{R}(\omega_x,\omega_z)\right|^2 + \lambda_2^{-1}\left|\mathbf{R}(-\omega_z,\omega_x)\right|^2 + \lambda_{\mathbf{P}}^{-1}} \quad (4.44)$$

4.3.5 Initialization and Constraints

Initialization

Similar to the case of the reflectivity image as the hidden data as described in section 4.2.5, the initial conditions $\boldsymbol{\theta}^{[0]}$ have a great effect on the ability of the EM algorithm to converge to a good estimation. Again, $\eta_{\mathbf{P}1}{}^{[0]}$ and $\eta_{\mathbf{P}2}{}^{[0]}$ should have the same value at all frequencies, the initialization for $\mathbf{R}^{[0]}$ should be the average of the RF images $\mathbf{S}_V$ and $\mathbf{S}_H$, and for the noise variance the initial estimate is higher than the true value.

Iterations

In each iteration of the algorithm the E-step is followed by the M-step:

1. The E-step consists of the evaluation of the expressions in (4.33), (4.34) (or alternatively (4.43), (4.44)) and (4.35), namely the expectation and variance of $\mathbf{P}_1(\omega_x,\, \omega_z)$ and $\mathbf{P}_2(\omega_x,\, \omega_z)$ are calculated using the parameter estimates from the previous M-step.
2. The M-step consists of the evaluation of the expressions in (4.38), (4.39) (or alternatively (4.42)), (4.40), (4.41), namely the new parameter estimates are calculated using the expectation and variance of $\mathbf{P}_1(\omega_x,\, \omega_z)$ and $\mathbf{P}_2(\omega_x,\, \omega_z)$ from the previous E-step.

These 2 steps can be performed in succession for a pre-defined number of iterations or until the change in $E[\mathbf{P}_1|\mathbf{s},\boldsymbol{\theta}^{[n]}]$ and $E[\mathbf{P}_2|\mathbf{s},\boldsymbol{\theta}^{[n]}]$ is small enough.

Scaling

Similar to section 4.2.5 we enforce every iteration $||E[\mathbf{P}_1|\mathbf{s},\boldsymbol{\theta}^{[n]}]||^2 = ||E[\mathbf{P}_2|\mathbf{s},\boldsymbol{\theta}^{[n]}]||^2 = N_{DFT}{}^2$.

Limiting the Conditional Variance

In the initial iterations the estimation of the variances λ_1, λ_2, $\lambda_{\mathbf{P}1}$ and $\lambda_{\mathbf{P}2}$ is unreliable. As a result the estimation in (4.38) is much improved if $Var[\mathbf{P}_{1,2}(\omega_x,\, \omega_z)|\mathbf{s},\boldsymbol{\theta}^{[n]}]$ are limited such that for any frequency pair $(\omega_x,\, \omega_z)$ its value is not too large or small relatively to max$|\, E[\mathbf{P}_1(\omega_x,\, \omega_z)|\mathbf{s},\boldsymbol{\theta}^{[n]}]\, |^2$ and max$|\, E[\mathbf{P}_2(\omega_x,\, \omega_z)|\mathbf{s},\boldsymbol{\theta}^{[n]}]\, |^2$ respectively.

Windowing In the Space Domain

Once more, multiplication of the estimated tissue reflectivity and blur PSF's by limiting window functions can suppress unwanted non-zero values. For more details see section 4.2.5.

Windowing In the Frequency Domain

Again, the estimated frequency response can be multiplied by a window function $\mathbf{W}(\omega_x, \omega_z)$ to suppress out-of-band frequencies. For example, if the same blur is assumed in both views, the conditional expectation in equation (4.43) can be modified as follows:

$$E[\mathbf{P}(\omega_x, \omega_z)|\mathbf{s},\boldsymbol{\theta}^{[n]}] = E[\mathbf{P}(\omega_x, \omega_z)|\mathbf{s},\boldsymbol{\theta}^{[n]}]\ \mathbf{W}^{[n+1]}(\omega_x, \omega_z)\ ,\ \forall \omega_x,\omega_z\ 0 \le \mathbf{W}^{[n+1]}(\omega_x, \omega_z) \le 1 \quad (4.45)$$

Note that the conditional variance $Var[\mathbf{P}(\omega_x, \omega_z)|\mathbf{s},\boldsymbol{\theta}^{[n]}]$ in equation (4.44) is not multiplied by $\{\mathbf{W}^{[n+1]}(\omega_x, \omega_z)\}^2$ otherwise in the following iterations there will be noise enhancement at frequencies where $\mathbf{W}(\omega)$ is relatively small. The window function can be like with the case of the reflectivity image as the hidden data as described in section 4.2.5.

4.4 Simulations

4.4.1 Simulation Description

We developed a Matlab simulation that tests the suggested methods under various circumstances: an assortment of tissue reflectivity maps, different noise levels and varied bandwidth of the system response.

Tissue Reflectivity Maps

We tested the algorithm with tissue reflectivity according to its model as the sum of deterministic and stochastic components. For the deterministic component we prepared several artificial maps; one of them is displayed in Figure 4.2. Their size is 512×512 pixels, which corresponds approximately with 20×20 mm for a sampling interval of 40 μm. For the stochastic component we added white Gaussian noise independently for each view direction.

(a) (b)

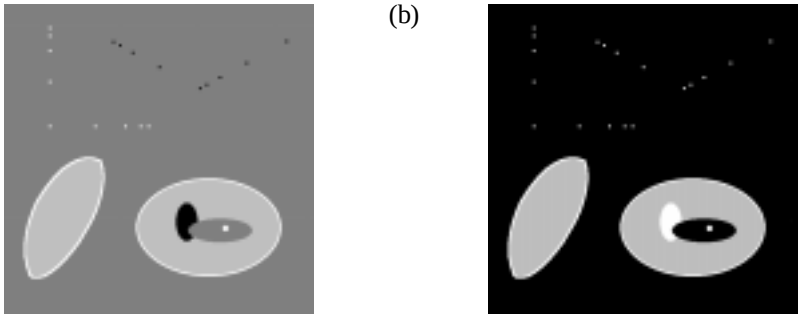

Figure 4.2: (a) A simulated reflectivity map. The 4 series of dots simulate wire targets that are separated by 0.5, 1, 2 and 3 mm. The mapping of colors is: black → -0.5, dark gray → 0, bright gray → 0.25 and white → 0.5. (b) The reflectivity map after log-compression

Degradation Process assuming 2-D LPF

We tested the algorithm first with LPF-type system response in both axial and lateral directions. We modeled the response as a two-dimensional separable filter with PSF:

$$\mathbf{P}(x, z) = \mathrm{sinc}^2(x/w_L)\ \exp(-|z/w_A|^2/2) \quad (4.46)$$

where w_L, w_A define the PSF width in each direction.

In the frequency domain this system response has in the ω_x direction a triangular shape with 99%-energy at $|\omega_x| \le 1.569\pi \frac{d_L}{w_L}$ radians, while in the ω_z direction it has a Gaussian shape with 99%-energy at $|\omega_z| \le 0.58\pi \frac{d_A}{w_A}$ radians. In the simulation we used the same system response for both views, with parameters: $d_L = d_A = 40$ μm, $w_L = 1.25$ mm, and $w_A = 0.115$ mm.

Degradation Process assuming 2-D Ultrasound-Type Blur

After establishing satisfactory results with the 2-D LPF, we tested the algorithm with a system response that is axially BPF and laterally LPF. We simulated this according to the non-separable model that was presented by Walker and Trahey in [24].

Walker and Trahey derived a model for the system response to a point target located in either the focus z_f or the far field of the transducer. They developed the following expression for representation of a typical imaging system with a transmit-receive axial frequency response $B_{TR}(\omega_z)$ and transmit and receive aperture weighting functions $L_T(x)$ and $L_R(x)$ respectively:

$$\mathbf{P}(\omega_x, \omega_z, 2z_f/v) = \frac{G}{\omega_z^2} B_{TR}(\omega_z)\, L_T(-2 z_f \omega_x/\omega_z) *_x L_R(-2 z_f \omega_x/\omega_z) *_x \mathrm{FT}_x\{\phi(x, \omega_z, z_f)\} \tag{4.47}$$

The symbol $*_x$ represents convoution in the lateral direction, and $\mathrm{FT}_x\{\}$ is the Fourier transform taken with respect to x. The term $\phi(x, \omega_z, z_f)$ in (4.47) is a quadratic phase curvature term that results from the spherical spreading of acoustic waves as they travel outward from the transducer:

$$\phi(x, \omega_z, z_f) = \exp(j\omega_z \frac{f_s}{v} \frac{|x|^2}{z_f}) \tag{4.48}$$

Taking the inverse Fourier transform (FT) of equation (4.47) yields:

$$\mathbf{P}(x, z) = \mathrm{IFT}\{\frac{G}{\omega_z^2} B_{TR}(\omega_z)\, L_T(-2 z_f \omega_x/\omega_z) *_x L_R(-2 z_f \omega_x/\omega_z)\} *_z \mathrm{IFT}_z\{\phi(x, \omega_z, z_f)\} \tag{4.49}$$

IFT{} dentoes 2-D inverse FT, and $\mathrm{IFT}_z\{\}$ is the inverse FT taken with respect to z.

In the simulation we used the same system response for both views, with the parameters: $d_L = d_A = 40$ μm, $z_f = 60$ mm, rectangular aperture weighting $L_T(x)$ and $L_R(x)$ having width of 25 mm, and a Gaussian axial frequency response $B_{TR}(\omega_z)$ with center frequency 0.4π rad (4 MHz) and $\sigma = 0.11\pi$ rad (1.1 MHz). The resulting PSF and spectrum are illustrated in Figure 3.1.

Log-Compression

For display purpose all the images passed conventional logarithmic compression:

$$\mathbf{A}_{\mathrm{Compressed}}(x, z) = b \log_2(a\, \mathbf{A}(x, z) + 1) \tag{4.50}$$

We used the values $a = 10$ and $b = N_{\mathrm{gray}} / \log_2(a + 1) = 256 / \log_2(11) = 74$, where N_{gray} is the number of gray levels from black to white. An example of a resulting pair of images appears in Figure 1.1.

4.4.2 Quality Measure

The above estimation methods of the system response cannot recover its scaling, i.e. the estimation can be accurate up to a gain factor. Therefore, in order to compare the estimated

response with the true one this factor should be estimated as well. We used the least squares method for this purpose:

$$J\{g\} = \sum_k \sum_l \left| g\hat{\mathbf{P}}(\omega_x, \omega_z) - \mathbf{P}(\omega_x, \omega_z) \right|^2 \tag{4.51}$$

$$g_{optimal} = \frac{\sum_k \sum_l \mathrm{Re}\left\{ \hat{\mathbf{P}}(\omega_x, \omega_z)^* \mathbf{P}(\omega_x, \omega_z) \right\}}{\sum_k \sum_l \left| \hat{\mathbf{P}}(\omega_x, \omega_z) \right|^2} \tag{4.52}$$

We used normalized mean squared error (MSE) as a quality metric to evaluate the system-response estimation:

$$\mathrm{MSE}\{\mathbf{P}\} = \frac{\sum_k \sum_l \left| g\hat{\mathbf{P}}(\omega_x, \omega_z) - \mathbf{P}(\omega_x, \omega_z) \right|^2}{\sum_k \sum_l \left| \mathbf{P}(\omega_x, \omega_z) \right|^2} \tag{4.53}$$

When using the gain according to (4.52) the MSE becomes

$$\mathrm{MSE}\{\mathbf{P}\} = 1 - \frac{\left[\sum_k \sum_l \mathrm{Re}\left\{ \hat{\mathbf{P}}(\omega_x, \omega_z)^* \mathbf{P}(\omega_x, \omega_z) \right\} \right]^2}{\sum_k \sum_l \left| \hat{\mathbf{P}}(\omega_x, \omega_z) \right|^2 \sum_k \sum_l \left| \mathbf{P}(\omega_x, \omega_z) \right|^2} = \tag{4.54}$$

$$= 1 - [\mathit{Correlation\text{-}Coefficient}\{\hat{\mathbf{P}}, \mathbf{P}\}]^2$$

4.4.3 Comparison of the Estimation Methods

When we simulated the EM methods we found out that the initial conditions have a great effect on the ability of the algorithm to converge to a good estimation. Our conclusion are described in sections 4.2.5 and 4.3.5. The variance of the noise is initialized as stated there to be higher than the true value, which is estimated from the average power of the RF images at a frequency range that is far from the pass-band of the imaging system.

Another important observation is that in both EM methods the use of constraints, especially the limiting and frequency-domain windowing, is critical for convergence and have significant influence on the estimation quality.

In the examples below the DFT length N_{DFT} is 1024 samples, and the required number of iterations is about 20 for both EM methods with the following constraints in use:

1. Space-domain window $\mathbf{\Omega_P}(x, z)$ that is applied to the blur as in equation (4.27). The window is the product of 2 raised cosines – one in the lateral direction having width of $^7/_{16}N_{DFT}$ samples and roll-off width of $^3/_{16}N_{DFT}$ samples, and the other in the axial direction having width of 1.375 times the axial length of the actual blur and roll-off width of 0.625 times that axial length.
2. Frequency-domain window as in (4.28) and (4.45). Here also 2 raised-cosine windows are used – in the lateral direction having 6 dB attenuation at $^7/_{32}\pi$ rad and roll-off width of $^5/_{16}\pi$ rad, and in the axial direction having 6 dB attenuation at 0.1π rad and 0.75π rad and roll-off width of 0.2π rad at its low-frequency end and 0.33π rad at its high-frequency end.

3. Limiting is enforced every iteration: For the case of the reflectivity as the hidden data – $0.001 \max|\mathbf{P}(\omega_x, \omega_z)|^2 \le \lambda/\lambda_u \le 0.25 \max|\mathbf{P}(\omega_x, \omega_z)|^2$; For the case of the blur as the hidden data the same factors limit $Var[\mathbf{P}(\omega_x, \omega_z)|\mathbf{s},\boldsymbol{\theta}]$ relative to $\max|E[\mathbf{P}(\omega_x, \omega_z)|\mathbf{s},\boldsymbol{\theta}]|^2$.

Figure 4.3 shows an example for the dependence of MSE{**P**} on the peak-to-speckle ratio for the reflectivity map that is displayed in Figure 4.2. The standard deviation of the noise is kept 6 dB below that of the speckle.

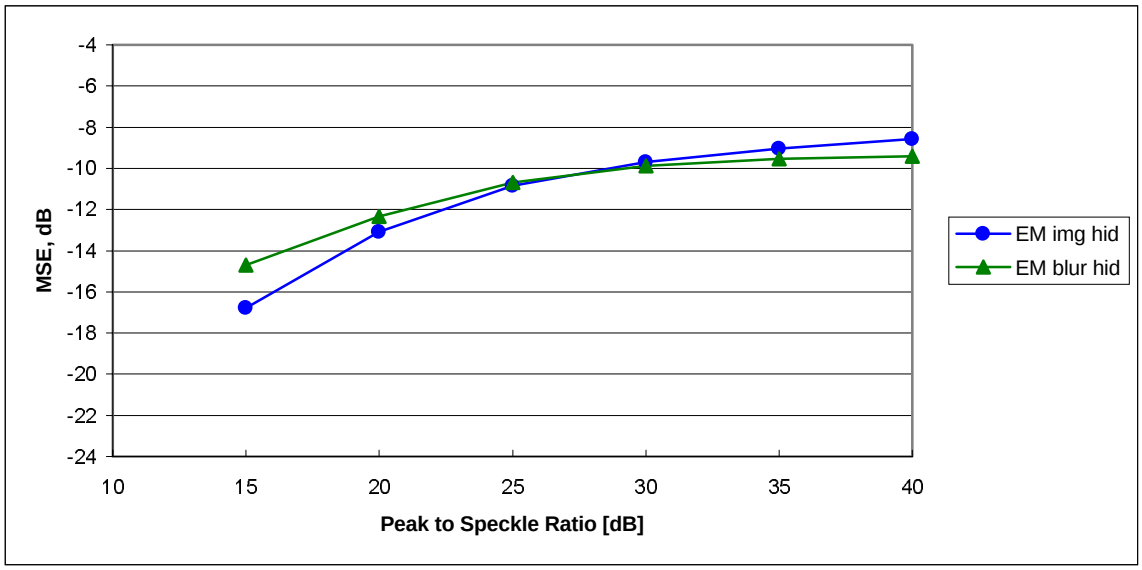

Figure 4.3: Dependence of MSE on peak-to-speckle ratio using the EM estimation methods

Figure 4.4 shows an example for the dependence of MSE{**P**}on the speckle-to-noise ratio. The standard deviation of the speckle is kept 30 dB below the peak value of the deterministic component of the tissue reflectivity. The reflectivity map for this example is again the map in Figure 4.2.

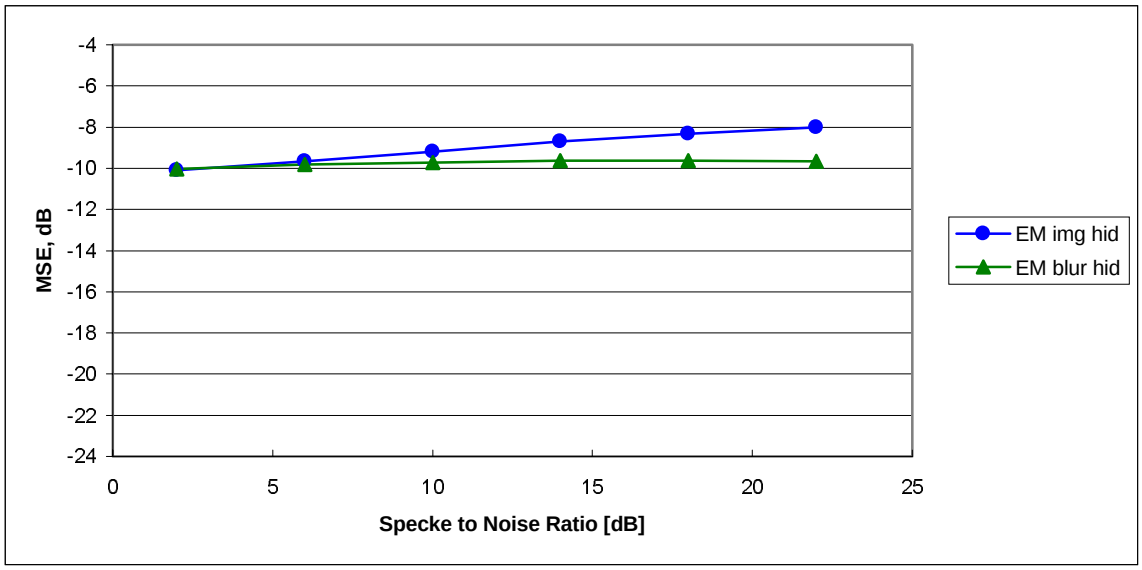

Figure 4.4: Dependence of MSE on speckle-to-noise ratio using the EM estimation methods

Figure 4.5 shows an example for the dependence of MSE{**P**} on the focus depth z_f, which influences the lateral width of the response through the term $L_T(-2\ z_f\ \omega_x/\omega_z) *_x L_R(-2\ z_f\ \omega_x/\omega_z)$. This dependence is checked at peak-to-speckle ratio of 30 dB and speckle-to-noise ratio of 6 dB. The reflectivity map for this example is also the map that is displayed in Figure 4.2. The constraints are the same as those for the example in Figures 4.3-4.4, except that the frequency-domain window is changed such that in the lateral direction its 6 dB bandwidth is in the range 0.188π-0.375π rad.

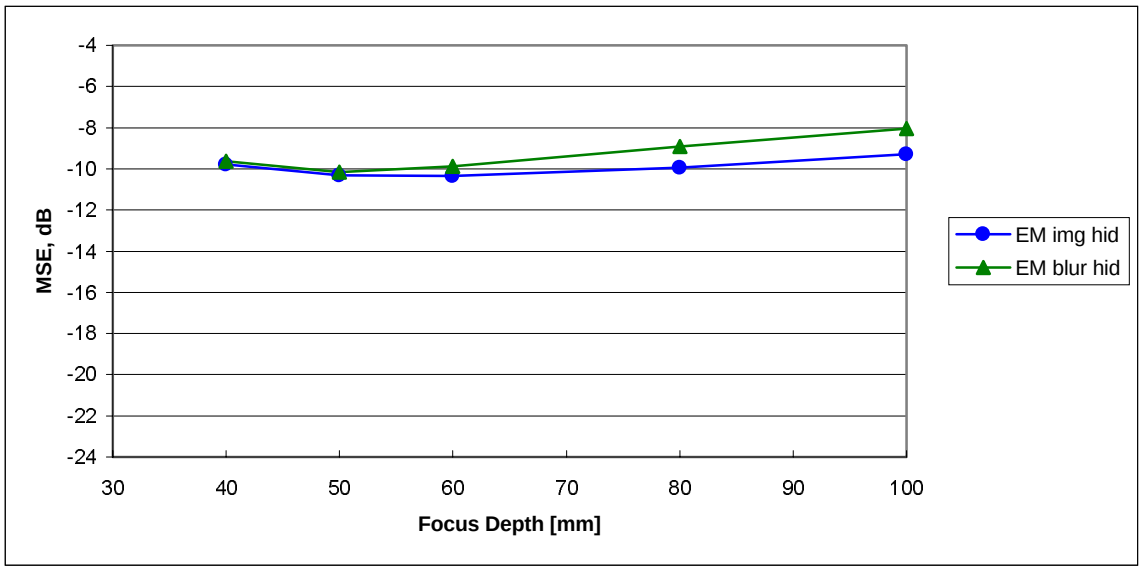

Figure 4.5: Dependence of MSE on focus depth using the EM estimation methods

5 Reflectivity-Image Reconstruction and Compounding

According to the approach of multi-channel image restoration [21] the restored image is taken from the last Expectation-Maximization iteration, i.e. from (4.11) or (4.38). However, in ultrasound imaging the resulting image would contain oscillations, as is the case with any ultrasound RF image, due to the band-pass character of the ultrasonic system. Consequently there would be required envelope detection.

When handling single RF images, where the oscillations are along just one axis, the envelope can be detected either through demodulation or through application of a Hilbert filter, followed by absolute value calculation. But, the image of (4.11) or (4.38) has oscillations along both axes, thus demodulation or Hilbert filtering cannot be utilized. See Figure 5.2.

5.1 Methods for Reconstruction and Spatial Compounding

The conclusion is that the compound image should be generated through one of the following methods, which are also illustrated in Figure 4.1:

Method A – Multi-channel reconstruction with envelope-detection

1. Calculation of the absolute value of the multi-channel restored image from (4.11) or (4.38).
2. Low-pass filtering of the resulting image.
3. Log-compression of the filtered image. See Figure 5.2.

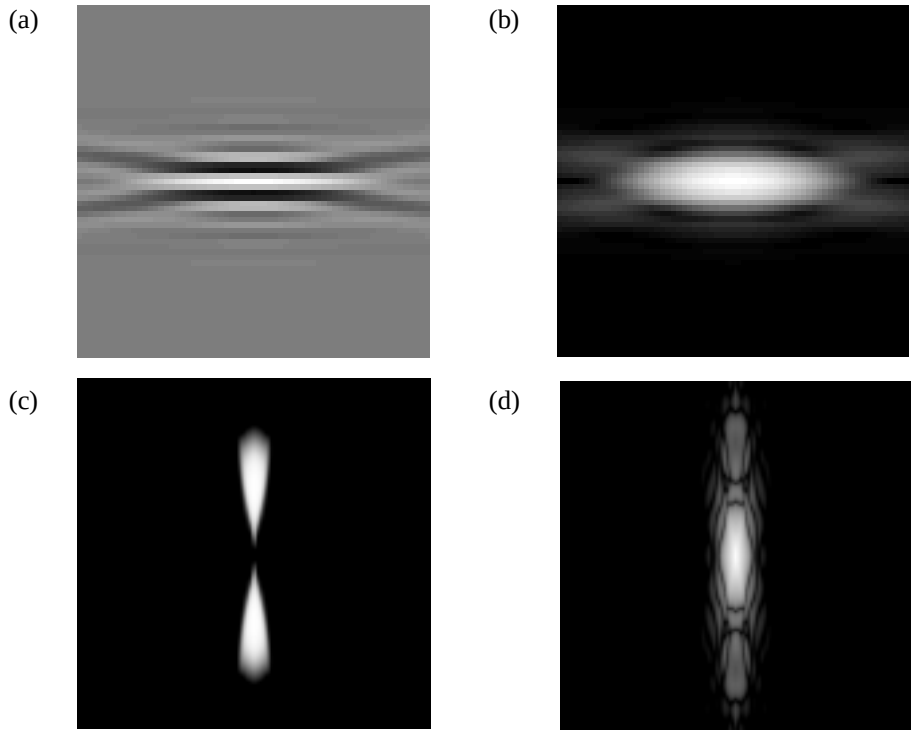

Figure 5.1: Simulation of an ultrasound scan of a wire target using the system response model in [24]:
(a) The RF image (axial direction along the vertical axis). (b) The envelope-detected image. The images in a and b are displayed after log-compression. The range of the space axes is [-0.64, 0.64] mm. (c)-(d) The spectrum of a-b respectively. The range of the frequency axes is $[-\pi, \pi]$ rad.

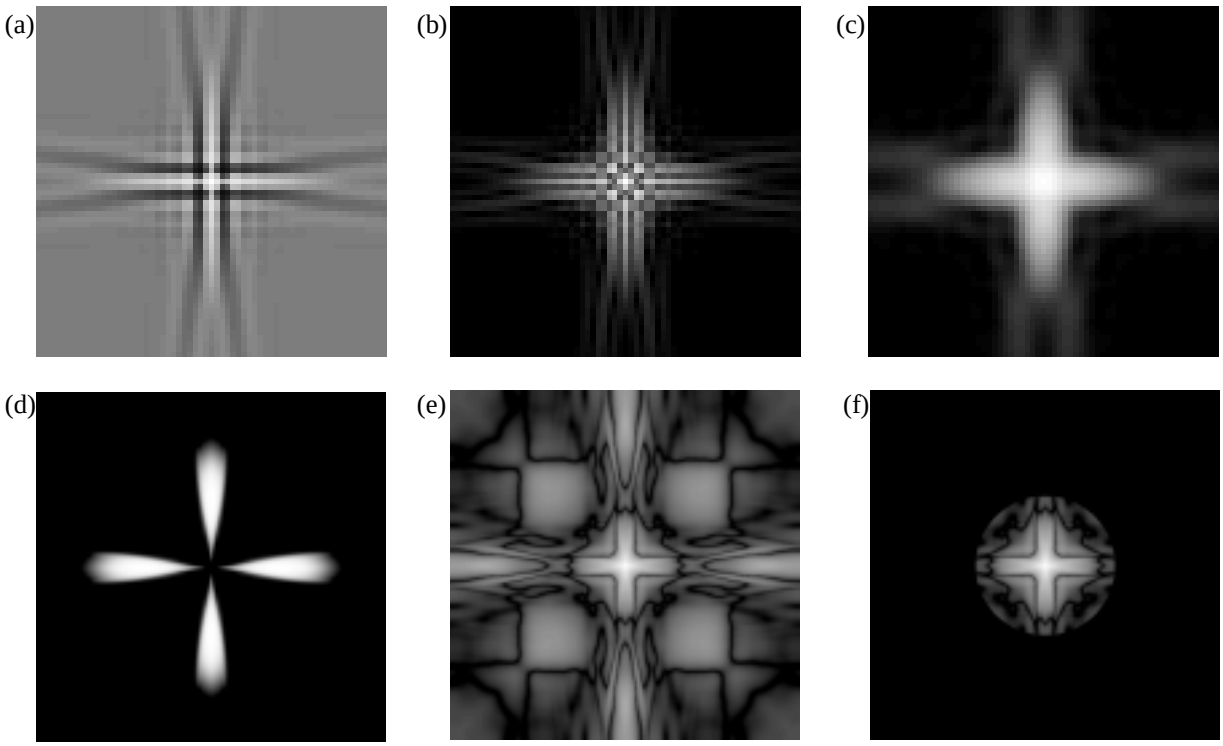

Figure 5.2: Multi-channel reconstruction with envelope-detection applied to the ultrasound scan in Figure 5.1:
(a) The multi-channel reconstruction. (b) The image after absolute value. (c) The image after LPF. The images in a-c are displayed after log-compression. The range of the space axes is [-0.64, 0.64] mm. (d)-(f) The spectrum of a-c respectively. The range of the frequency axes is $[-\pi, \pi]$ rad.

Method B – Separate reconstruction with averaging

1. Calculation of the 2 separate Wiener filter solutions using (4.11) or (4.38) and substituting 0 for λ_u and λ_1^{-1} or λ_2^{-1} respectively.
2. Envelope detection of each resulting image.
3. Averaging (see Figure 5.3), such as:
   a. Averaging of the 2 envelope detected images followed by log-compression.
   b. Log-compression of the 2 envelope detected images followed by averaging.

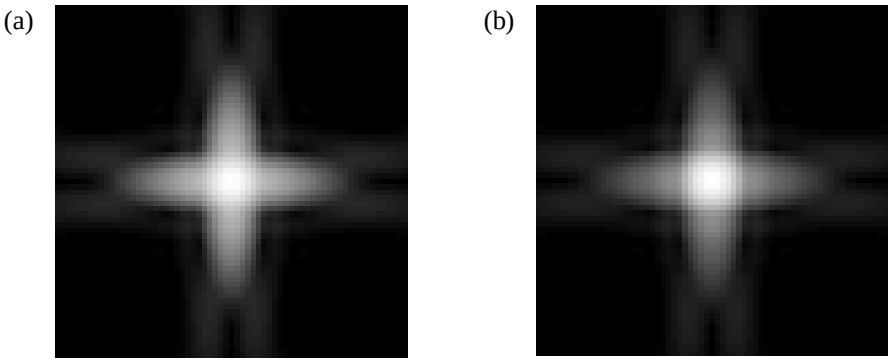

Figure 5.3: Separate reconstruction with averaging applied to the ultrasound scan in Figure 5.1:
(a) Averaging before log-compression. (b) Averaging after log-compression. The range of the space axes is [-0.64, 0.64] mm.

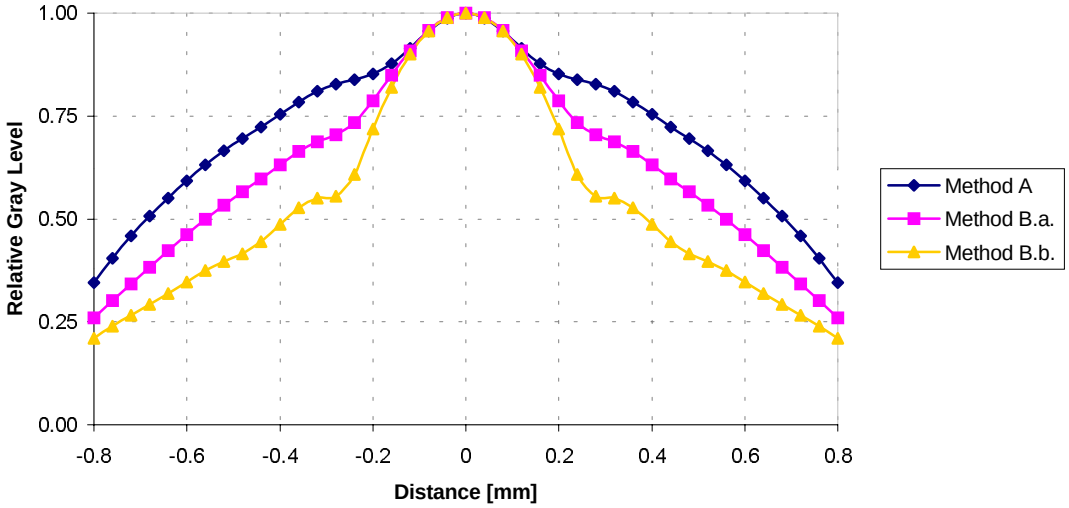

Figure 5.4: Horizontal section through the center of the reconstructed images in Figure 5.2 (f) denoted as "Method A", Figure 5.3 (a) denoted as "Method B.a" and Figure 5.3 (b) denoted as "Method B.b".

5.2 Simulations

We compared 4 types of reconstruction of the reflectivity map:

1. Multi-channel reconstruction with envelope-detection. This is method A in section 5.1.
2. Separate reconstructions, then averaging before log-compression. This is method B.a. in section 5.1.

3. Separate reconstructions, then averaging after log-compression. This is method B.b. in section 5.1.
4. A simple average after log-compression. This is the most naïve way, and it serves as a lower bound for the possible quality of reconstruction.

Figures 5.5 and 5.6 show reconstructed images using these types of reconstruction. Both examples are with peak-to-speckle ratio of 25 dB and speckle-to-noise ratio of 6 dB.

The conclusion from the examples in sections 5.1 and 5.2 is that the method of separate reconstruction with averaging after log-compression has the best ability to separate close small objects such as wire targets while multi-channel reconstruction with envelope-detection gives the greatest suppression of noise and speckle. These two methods have a similar increase in sharpness of the display for large or lengthy objects.

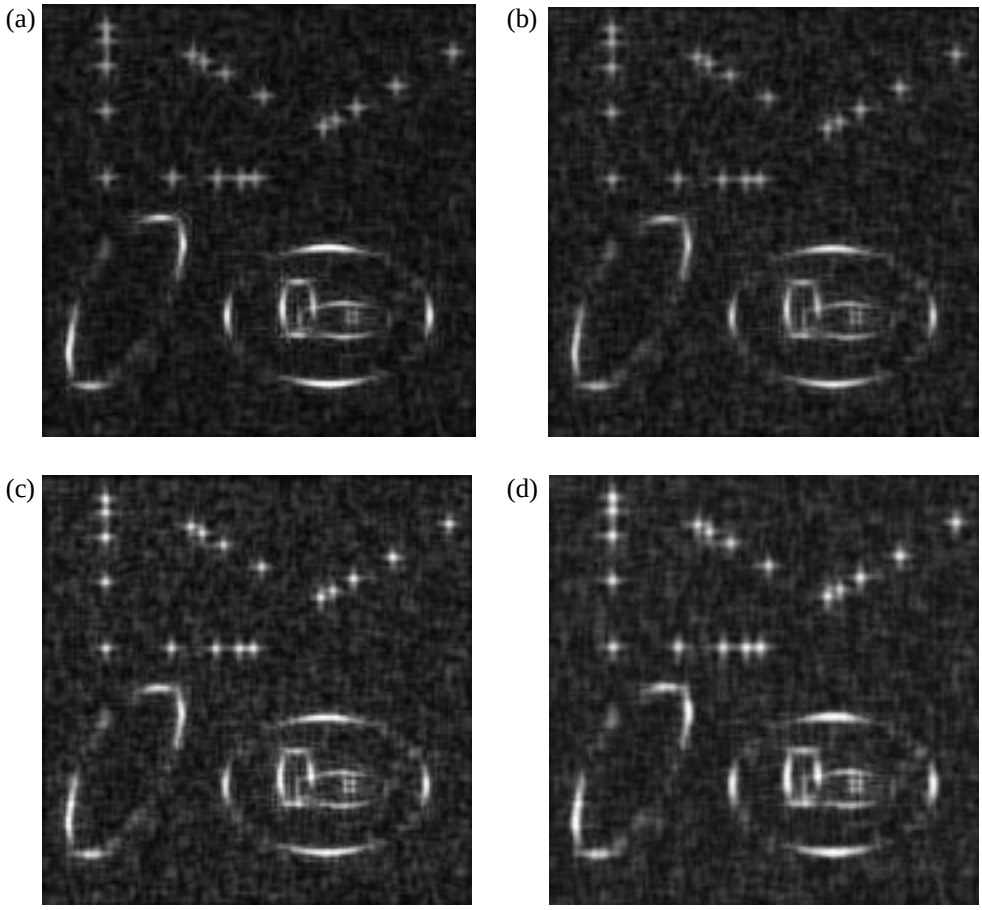

Figure 5.5: Comparison of methods for image reconstruction and compounding: (a) Multi-channel reconstruction with envelope-detection (b) Separate reconstructions, then averaging before log-compression (c) Separate reconstructions, then averaging after log-compression. (d) A simple average after log-compression.

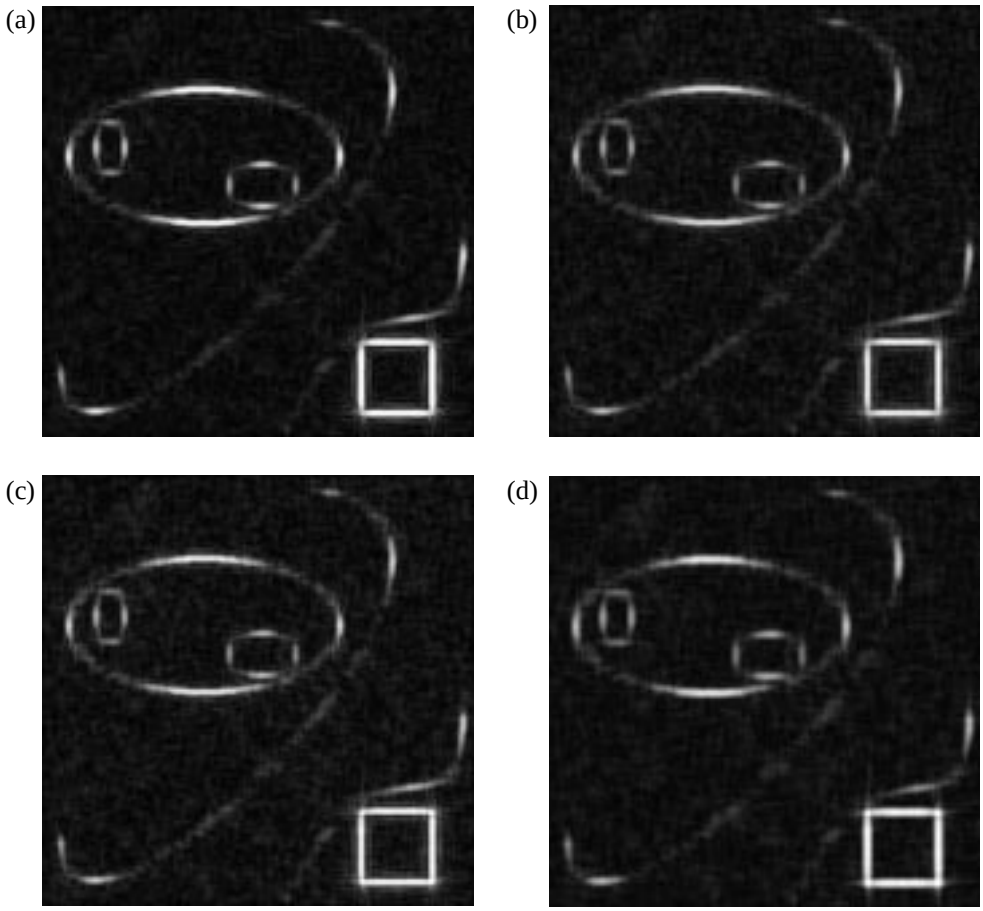

Figure 5.6: Comparison of methods for image reconstruction and compounding: (a) Multi-channel reconstruction with envelope-detection (b) Separate reconstructions, with averaging before log-compression (c) Separate reconstructions, with averaging after log-compression. (d) A simple average after log-compression.

6 Conclusions and Discussion

In this research we developed a new method to exploit pairs of ultrasound scans of the same plane in order to achieve an enhanced ultrasound image compared to images from single scans. Each pair is assumed to consist of two co-registered image with 90° separation between their insonification directions. Former researches in the field of ultrasound imaging dealt with the tasks of blind deconvolution and spatial compounding independently, while this study combines these tasks through the approach of multi-channel image restoration that is borrowed from the field of photographic imaging.

The algorithm that we developed performs first blind identification of the ultrasonic system parameters and then spatial compounding of the ultrasound scans. For the identification task this algorithm adopts the approach of multi-channel image restoration as it can be viewed as an individual case with a single source image that passes through 2 different channels. For spatial compounding in the case of ultrasound imaging with 90° separated views, we demonstrated that averaging after envelope detection can be more suitable for improvement of resolution than using the restored image from the multi-channel image restoration algorithm.

Our experiments show that the parameter identification is robust to changes in the relative level of speckle or white noise as well as in the spectral shape of the system response. In order to achieve adequate performance the algorithm requires some constraints, such as limiting the

noise-to-speckle ratio, windowing in the space and frequency domains [26], [27] and limiting the number of iterations. These constraints need to be tuned for the specific ultrasonic system where the parameter identification is performed. The simulations also suggest that using the estimated parameters for image restoration can enhance the quality of the compound image compared to the approach of algebraic average without Wiener filtering.

Future research can be carried out so as to adjust the algorithm for multiple scans with angular separation smaller than 90°. The 2 alternatives are to rotate the transducer around a fixed point within the imaged tissue in steps that are smaller than 90° as illustrated in Figure 6.1(a) or to steer the ultrasonic beam so as to collect a set of scans at various angles as illustrated in Figure 6.1(b). The advantage of the second scheme is that it does not have a registration problem since the transducer is not moved between scans at different angles.

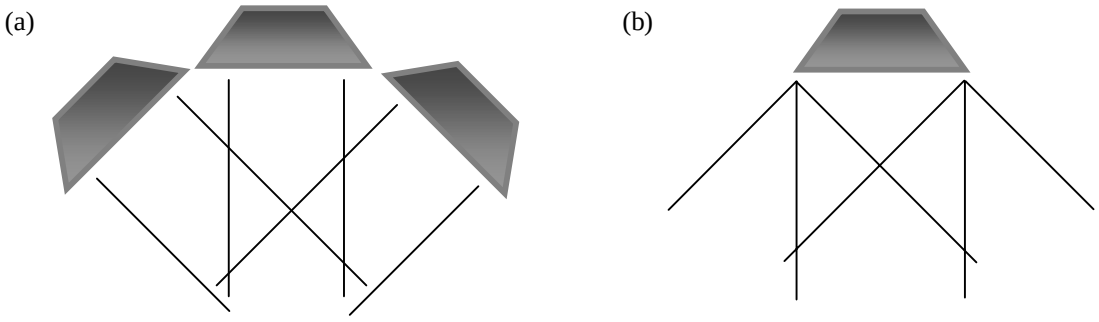

Figure 6.1: Illustration of compounding schemes with angular separation smaller than 90°:
(a) Rotating the transducer around a fixed point within the imaged tissue.
(b) Steering the ultrasonic beam so as to collect a set of scans at various angles.

Another interesting option is to modify the algorithm to deal with spatial compounding of sector scans instead of linear array scans (polar r-θ coordinates rather than Cartesian x-z coordinates), as illustrated in Figure 6.2. A possible advantage of sector scans is improved spatial invariance in the polar coordinate representation [5].

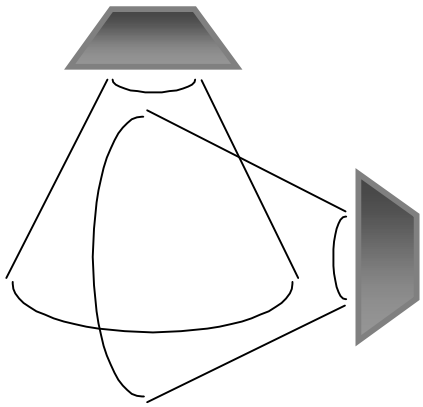

Figure 6.2: Illustration of sector scan compounding.

Finally, the current algorithm assumes that there are no spatial deformations in the RF images due to variations in the speed of sound. In practice there might be cases when such deformations cannot be neglected. Therefore, it is desirable to incorporate an algorithm for estimation and compensation for the deformation into the process of parameter identification, image restoration and compounding [16].

Acknowledgments

This research was supported in part by the HASSIP Research Program HPRN-CT-2002-00285 of the European Commission, and by the Ollendorff Minerva Center. Minerva is funded through the BMBF. YK is grateful to Micha Anholt for his assistance along this project. MP would like to thank Dr. Moshe Bronstein for his contribution to this research.

References

1. E.E. Hundt and E.A. Trautenberg, "Digital Processing of Ultrasonic Data by Deconvolution", *IEEE Trans. Sonics. Ultrason.*, vol. 27, no. 5, pp. 249-252, Sep. 1980.
2. C.N. Liu, M. Fatemi and R.C. Waag, "Digital Processing for Improvement of Ultrasonic Abdominal Images", *IEEE Trans. Med. Imaging.*, vol. 2, no. 2, pp. 66-75, June 1983.
3. J.A. Jensen and S. Leeman, "Nonparametric Estimation of Ultrasound Pulses", *IEEE Trans. Biomed. Eng.*, vol. 41, no. 10, pp. 929-936, Oct. 1994.
4. J.A. Jensen, "Estimation of In Vivo Pulses in Medical Ultrasound", *Ultrasonic Imaging*, vol. 16, pp. 190-203, 1994.
5. T. Taxt, "Restoration of Medical Ultrasound Images Using Two-Dimensional Homomorphic Deconvolution", *IEEE Trans. Ultrason., Ferroelect., Freq. Contr.*, vol. 42, no. 4, pp. 543-554, July 1995.
6. U.R. Abeyratne, A.P. Petropulu and J.M. Reid, "Higher Order Spectra Based Deconvolution of Ultrasound Images", *IEEE Trans. Ultrason., Ferroelect., Freq. Contr.*, vol. 42, no. 6, pp. 1064-1075, Nov. 1995.
7. J.H. Hokland and P.A. Kelly, "Markov Models of Specular and Diffuse Scattering in Restoration of Medical Ultrasound Images", *IEEE Trans. Ultrason., Ferroelect., Freq. Contr.*, vol. 43, no. 4, pp. 660-669, July 1996.
8. T. Taxt and G.V. Frolova, "Noise Robust One-Dimensional Blind Deconvolution of Medical Ultrasound Images", *IEEE Trans. Ultrason., Ferroelect., Freq. Contr.*, vol. 46, no. 2, pp. 291-299, Mar. 1999.
9. T. Taxt and J. Strand, "Two-Dimensional Noise-Robust Blind Deconvolution of Ultrasound Images", *IEEE Trans. Ultrason., Ferroelect., Freq. Contr.*, vol. 48, no. 4, pp. 861-866, July 2001.
10. D. Adam and O. Michailovich, "Blind Deconvolution of Ultrasound Sequences Using Nonparametric Local Polynomial Estimates of the Pulse", *IEEE Trans. Biomed. Eng.*, vol. 49, no. 2, pp. 118-131, Feb. 2002.
11. P. He, K. Xue, Q. Chen, P. Murka and S. Schall, "A PC-Based Ultrasonic Data Acquisition System for Computer-Aided Prosthetic Socket Design", *IEEE Trans. Rehabil. Eng.*, vol. 4, no. 2, pp. 114-119, June 1996.
12. P. He, K. Xue and Y. Wang, "Effects of Spatial Compounding Upon Image Resolution", *Proc.* 19th *Int. Conf. IEEE Eng. Medic. Bio. Society*, pp. 598-600, Oct. 1997.
13. S.K. Jespersen, J.E. Wilhjelm and H. Sillesen, "Ultrasound Spatial Compound Scanner for Improved Visualization in Vascular Imaging", 1998 *IEEE Ultrason. Symposium*, pp. 1623-1626, 1998.

14. D.F. Leotta and R.W. Martin, “Three-Dimensional Spatial Compounding of Ultrasound Scans with Incidence Angle Weighting”, 1999 *IEEE Ultrason. Symposium*, pp. 1605-1608, 1999.

15. J.E. Wilhjelm, M. S. Jensen, T. Brandt, B. Sahl, K. Martinsen, S.K. Jespersen and E. Falk, “Some Imaging Strategies in Multi-Angle Spatial Compounding”, 2000 *IEEE Ultrason. Symposium*, pp. 1615-1618, 2000.

16. A. Shenhar and M. Porat, “A Dual Transducer Approach to Ultrasound Imaging and Spatial Deformations”, *Proc. IEEE 2000 Int. Conf. Image Processing*, vol. 1, pp. 10-13, Sep. 2000.

17. A. Shenhar, “Processing of Spatial Distortions in Images”, M.Sc. Thesis, Technion Israel Institute of Technology, 2001.

18. D.C. Ghiglia, “Space-Invariant Deblurring Given *N* Independently Blurred Images of a Common Object”, *J. Opt. Soc. Amer. A*, vol. 1, no. 4, pp. 398-402, April 1984.

19. A.K. Katsaggelos, K.T. Lay and N.P. Galatsanos, “A General Framework for Frequency Domain Multi-channel Signal Processing”, *IEEE Trans. Image Proc.*, vol. 2, no. 3, pp. 417-420, July 1993.

20. J.M. Links, J.L. Prince and S.N. Gupta, “A vector Wiener filter for dual-radionuclide imaging”, *IEEE Trans. Med. Imaging*, vol. 15, no. 5, pp. 700-709, Oct. 1996.

21. B.C. Tom, K.T. Lay and A.K. Katsaggelos, “Multichannel Image Identification and Restoration using the Expectation-Maximization Algorithm”, *Opt. Eng.*, vol. 35, no. 1, pp. 241-254, Jan. 1996.

22. J.U. Quistgaard, “Signal Acquisition and Processing in Medical Diagnostic Ultrasound”, *IEEE Sig. Proc. Mag.*, vol. 27, no. 1, pp. 67-74, Jan. 1997.

23. D. Iraca, L. Landini and L. Verrazzani, “Power Spectrum Equalization for Ultrasonic Image Restoration”, *IEEE Trans. Ultrason., Ferroelect., Freq. Contr.*, vol. 36, no. 2, pp. 216-222, March 1989.

24. W.F. Walker and G.E. Trahey, “The Application of K-space in Pulse Echo Ultrasound”, *IEEE Trans. Ultrason., Ferroelect., Freq. Contr.*, vol. 45, no. 3, pp. 541-558, May 1998.

25. T.K. Moon, “The Expectation-Maximization Algorithm”, *IEEE Signal Processing Magazine*, vol. 13 issue 6, pp. 47-60, Nov. 1996.

26. S. Urieli, M. Porat and N. Cohen, "Optimal Reconstruction of Images from Localized Phase", *IEEE Trans. on Image Processing*, Vol. 7, No. 6, pp. 838-853, 1998.

27. M. Porat and G. Shachor, "Signal Representation in the combined Phase - Spatial space: Reconstruction and Criteria for Uniqueness", *IEEE Trans. on Signal Processing*, Vol. 47, No. 6, pp. 1701-1707, 1999.